Geophys. J. Int. (2007) **170,** 1262–1288 doi: 10.1111/j.1365-246X.2007.03475.x

Upper-mantle flow beneath French Polynesia from shear wave splitting

Fabrice R. Fontaine,[1,2] Guilhem Barruol,[1,3] Andréa Tommasi[3] and Götz H. R. Bokelmann[3]

[1] *Laboratoire Terre-Océan, Université de Polynésie française,* BP 6570*,* 98702 *Faaa, Tahiti, Polynésie française*
[2] *Research School of Earth Sciences, Australian National University, Building 61, Mills Road, Canberra,* ACT 0200*, Australia. E-mail: fabrice@rses.anu.edu.au*
[3] *Géosciences Montpellier, CNRS, Université Montpellier II,* F-34095 *Montpellier Cedex 5, France*

Accepted 2007 April 23. Received 2007 April 23; in original form 2006 July 16

SUMMARY

Upper-mantle flow beneath the South Pacific is investigated by analysing shear wave splitting parameters at eight permanent long-period and broad-band seismic stations and 10 broad-band stations deployed in French Polynesia from 2001 to 2005 in the framework of the Polynesian Lithosphere and Upper Mantle Experiment (PLUME). Despite the small number of events and the rather poor backazimuthal coverage due to the geographical distribution of the natural seismicity, upper-mantle seismic anisotropy has been detected at all stations except at Tahiti where two permanent stations with 15 yr of data show an apparent isotropy. The median value of fast polarization azimuths (N67.5°W) is parallel to the present Pacific absolute plate motion direction in French Polynesia (APM: N67°W). This suggests that the observed SKS fast polarization directions result mainly from olivine crystal preferred orientations produced by deformation in the sublithospheric mantle due to viscous entrainment by the moving Pacific Plate and preserved in the lithosphere as the plate cools. However, analysis of individual measurements highlights variations of splitting parameters with event backazimuth that imply an actual upper-mantle structure more complex than a single anisotropic layer with horizontal fast axis. A forward approach shows that a two-layer structure of anisotropy beneath French Polynesia better explains the splitting observations than a single anisotropic layer. Second-order variations in the measurements may also indicate the presence of small-scale lateral heterogeneities. The influence of plumes or fracture zones within the studied area does not appear to dominate the large-scale anisotropy pattern but may explain these second-order splitting variations across the network.

Key words: French polynesia, seismic anisotropy, shear wave splitting, upper mantle.

1 INTRODUCTION

The Pacific Plate, which is almost entirely of oceanic origin, is one of the largest and fastest-moving plates of our planet. The structure of oceanic lithosphere should in principle be controlled by the interplay between cooling and thickening and the deformation induced at the base of the lithosphere by the motion of the plate relative to the deeper mantle (Schubert *et al.* 1976; Tommasi 1998). However, the small-scale structure of the upper mantle beneath the Pacific is not yet well known, due to the difficulty in deploying geophysical instruments in remote oceanic environments. In particular, there is a lack of permanent seismic stations providing the necessary observations to determine accurate upper-mantle tomographic images, to map the mantle flow, or to measure the depth of the major discontinuities. Global and regional surface wave tomographic models (e.g. Nishimura & Forsyth 1989; Montagner & Tanimoto 1991; Ekström & Dziewonski 1998; Montagner 2002; Maggi *et al.* 2006a,b), body wave global tomographic models (e.g. Grand *et al.* 1997; van der Hilst *et al.* 1997; Montelli *et al.* 2004) and bathymetric data (Smith & Sandwell 1994; Jordahl *et al.* 2004) have indeed rather poor resolution in the South Pacific. Although information on mantle plumes location has been derived from the analysis of volcanic structures and lineaments (e.g. Duncan & Richards 1991; Clouard & Bonneville 2005), the depth origin of these plumes and their effect on the overlying lithosphere are also still debated.

In order to constrain the structure of the South Pacific upper mantle, we deployed a temporary network of 10 broad-band three-component seismic stations on French Polynesia Islands (Fig. 1) in the frame of the Polynesian Lithosphere and Upper Mantle Experiment (PLUME) (Barruol *et al.* 2002). This South Pacific region is of particular interest since it lies far from any plate boundary, and it is large enough to sample oceanic lithosphere with ages varying

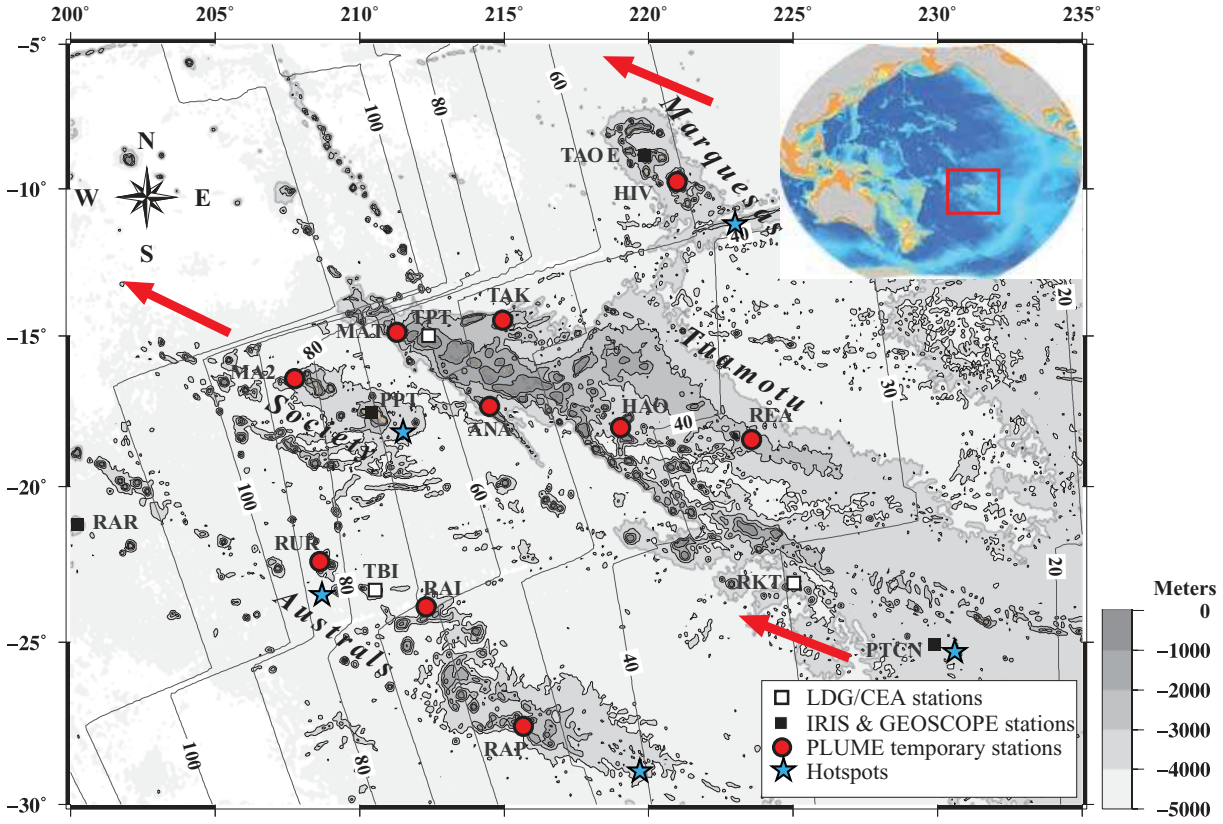

Figure 1. Bathymetric map of the French Polynesia area, showing the temporary PLUME network (circles) and the permanent stations from the IRIS, GEOSCOPE (black squares) and LDG/CEA networks (white squares). The age of the lithosphere and the vector of the Pacific absolute plate motion are also indicated. Stars show the hotspot locations.

between 30 and 100 Ma, as well as two major fracture zones, the Austral and Marquesas Fracture Zones. Moreover, the French Polynesia area is characterized by several volcanic island chains—the Society, Austral, Gambier and Marquesas archipelagos, that may represent hotspot tracks (Duncan & McDougall 1976; Clouard & Bonneville 2005). These volcanic alignments are superimposed on the large South Pacific Superswell (McNutt *et al.* 1996; McNutt 1998), characterized at the Earth's surface by a large-scale bathymetric anomaly (Sichoix *et al.* 1998; Adam & Bonneville 2005), and at depth by a large-scale, low-velocity anomaly in the lowermost mantle (Su *et al.* 1994; Mégnin & Romanowicz 2000). French Polynesia is, therefore, a unique area to study an oceanic plate affected by several plumes and to analyse the effect of plume activity on the lithosphere and asthenosphere structure and dynamics.

We focus in this paper on the mantle deformation that can be mapped beneath each seismic station by measuring the polarization anisotropy of teleseismic shear waves (e.g. Vinnik *et al.* 1984; Silver & Chan 1988; Silver & Chan 1991; Vinnik *et al.* 1992). Seismic anisotropy in the upper mantle is broadly accepted to result from intrinsic elastic anisotropy of rock-forming minerals—particularly olivine in the upper mantle—and from their preferred orientations, which develop in response to tectonic flow (Nicolas & Christensen 1987; Mainprice *et al.* 2000). A direct way to measure the upper-mantle seismic anisotropy at the Earth's surface is to use the splitting of teleseismic shear waves: a polarized shear wave propagating in an anisotropic medium is split into two perpendicularly polarized waves that travel at different velocities. Two parameters of anisotropy can be retrieved from three-component seismic records: the difference in arrival time (δt) between the two split shear waves, which depends on the thickness and on the intrinsic anisotropy of the medium, and the azimuth Φ of the fast split shear wave polarization planes, which is related to the orientation of the anisotropic structure. Measurement of teleseismic shear wave splitting can, therefore, be used to probe frozen or active mantle deformation beneath a station, with a lateral resolution of a few tens of kilometres and may provide crucial information on the past and present geodynamic processes that occurred in the oceanic upper mantle.

The PLUME experiment allowed us to investigate the upper-mantle flow beneath the South Pacific Superswell by performing new splitting measurements of teleseismic shear phases in this until now poorly instrumented region. In this paper, we present and examine the observations of shear wave splitting from both temporary stations of the PLUME deployment and permanent stations in the South Pacific, and put them in relation with expected directions for asthenospheric flow, mantle plumes, small-scale convection and fossil anisotropy. We also discuss the potential presence and characteristics of two layers of anisotropy beneath the South Pacific.

2 EXPERIMENT, DATA AND METHODOLOGY

2.1 Permanent and temporary stations: the PLUME's setup

In late 2001 we deployed a network of 10 broad-band seismic stations as part of the PLUME experiment (see locations Fig. 1 and Table 1). These stations remained operational until August 2005. This deployment completes the broad-band seismic coverage in the

Table 1. Station location and mean splitting parameters, as calculated by the Silver & Chan (1991) method and determined by the stacking method of Wolfe & Silver (1998)

Station	Latitude (°)	Longitude (°)	Wolfe & Silver						Silver & Chan				
			Φ (°)	σ_Φ (°)	δt (s)	$\sigma_{\delta t}$ (s)	Event no.	*df*	Φ (°)	σ_Φ (°)	δt (s)	$\sigma_{\delta t}$ (s)	Event no.
PTCN	−25.0714	−130.0953	−87	5	0.83	0.10	6	70	−84	7	1.09	0.10	5
RAR	−21.2125	−159.7733	−45	9	0.75	0.15	6	89	−63	8	1.71	0.22	5
RPN	−27.1267	−109.3344	−16	7	0.75	0.15	10	105	33	6	1.37	0.23	7
PPT	−17.5690	−149.5760	–	–	–	–	4	44	–	–	–	–	0
RKT	−23.1197	−134.9733	−55	9	1.10	0.15	7	144	−54	4	1.23	0.09	10
TPT	−14.9844	−147.6197	−63	9	0.90	0.28	3	30	−56	5	2.70	0.40	1
TBI	−23.3489	−149.4608	−80	5	1.10	0.18	5	38	−77	6	1.10	0.21	7
ANA	−17.3558	−145.5089	−44	5	0.88	0.14	5	89	−54	5	1.31	0.13	4
HAO	−18.0625	−140.9622	−75	9	0.70	0.18	5	59	−66	7	1.30	0.11	7
HIV	−9.7650	−139.0069	57	3	0.75	0.18	4	49	74	18	1.13	0.69	1
MAT	−14.8703	−148.7117	−72	12	0.65	0.23	4	60	−67	10	1.88	0.49	1
MA2	−16.4494	−152.2675	77	16	1.00	0.36	3	29	72	5	1.27	0.33	1
RAI	−23.8678	−147.6867	−46	14	1.18	0.41	2	29	−68	12	1.42	0.07	2
RAP	−27.6183	−144.3347	−71	9	0.80	0.21	5	56	−65	9	1.35	0.33	2
REA	−18.4636	−136.4442	79	3	1.35	0.11	5	45	89	6	1.52	0.15	5
RUR	−22.4325	−151.3686	83	3	0.80	0.11	5	87	−62	11	1.05	0.24	1
TAK	−14.4742	−145.0375	−67	19	0.63	0.28	4	45	−79	13	1.42	0.20	3

Notes: The number of events taken into account is also listed. *df* is the number of degrees of freedom computed from the data with the method of Wolfe & Silver (1998).

South Pacific provided by IRIS stations (RPN on Easter Island, RAR in the Cook Islands and PTCN on Pitcairn Island), GEOSCOPE stations PPT in Tahiti and TAOE in the Marquesas (installed in November 2004) and by the long-period stations operated in French Polynesia by the Laboratoire de Géophysique du Commissariat à l'Energie Atomique (hereafter called LDG/CEA): RKT on Mangareva in the Gambier Islands, TPT on Rangiroa in the Tuamotu archipelago, TBI on Tubuai in the Cook-Austral Island chain and PPTL on Tahiti.

2.2 Data availability and selection

In order to observe distinct, high signal-to-noise ratio SKS and SKKS phases, we selected teleseismic events located at distances larger than 85° and of magnitude generally greater than 5.8. The origins and locations of the events used in this study, which are reported in Tables 2 and 3, are taken from the U.S. Geological Survey (USGS) Preliminary Determination of Epicenters. Phase arrivals are computed using the IASP91 Earth reference model (Kennett & Engdahl 1991).

Although French Polynesia is surrounded by the seismicity generated by the circum-Pacific subduction zones, it lies in an unfavourable location for studies of core phases since most events occur at epicentral distances smaller than 85°. To illustrate and quantify this limitation, we present in Fig. 2(a) the number of SKS events that can potentially be used for splitting studies at any place in the world. This representation is for the events during the year 2002 that have magnitudes larger than 6.0 and that are occurring at epicentral distances in the range between 85° and 120°. The pattern is rather similar for different years. The North American Plate appears to be the best-placed continental area for performing SKS splitting studies. On the other hand, the most challenging places for SKS splitting studies are located along the Western Pacific subduction zones and around the southern Atlantic Ocean, with less than 20 events by year. The Southern Pacific Ocean appears to be poorly covered, with less than 30 events potentially available each year for SKS splitting measurements.

Beside having a sufficient number of events, it is also important for SKS splitting studies to have a reasonable backazimuthal coverage since it helps to characterize the homogeneity of the anisotropic structure beneath the station and the presence of several layers of anisotropy, if any. We present in Fig. 2(b) the location of the events on which we performed shear wave splitting measurements, together with the 85° and 120° epicentral distance (optimum distance range to get energetic and clear individual core shear phases) to two important stations in the South Pacific area: Tahiti (PPT) and Pitcairn Island (PTCN). These great circles clearly show that most of the events that fulfill this condition are located in the western and northwestern Pacific. The South American subduction is too close to our network and only part of the Caribbean and the South Sandwich subduction zones are within the 85–120° distance window, at least for the westernmost station of the network. Events occurring in the Philippines, Java, Japan trenches arrive in French Polynesia from W to NW backazimuths. Some rare events occurring in the Sandwich subduction zone provided some SE backazimuths. In summary, French Polynesia is characterized by rather poor backazimuthal coverage, with primary sampling of the NW quadrant. This observation is consistent with the result from Chevrot (2000). His map of the normalized azimuthal coverage for epicentral distance between 90° and 145° for every location at the surface of the Earth shows that French Polynesia is not in a favourable region for obtaining good backazimuthal coverage. In the following analysis of the measurements, we will see that this coverage directly results in a large number of 'null' splitting measurements, that is, events for which the energy of the SKS phase appears to be restricted to the radial component, and a rather low number of observed split shear waves.

2.3 Single and multi-event analysis

In order to compensate for the small number of events available for shear wave splitting measurements, but also for the rather high noise level present on oceanic island stations, we determine the anisotropic parameters beneath the various stations by two different approaches: (i) the single event method (Silver & Chan 1991)

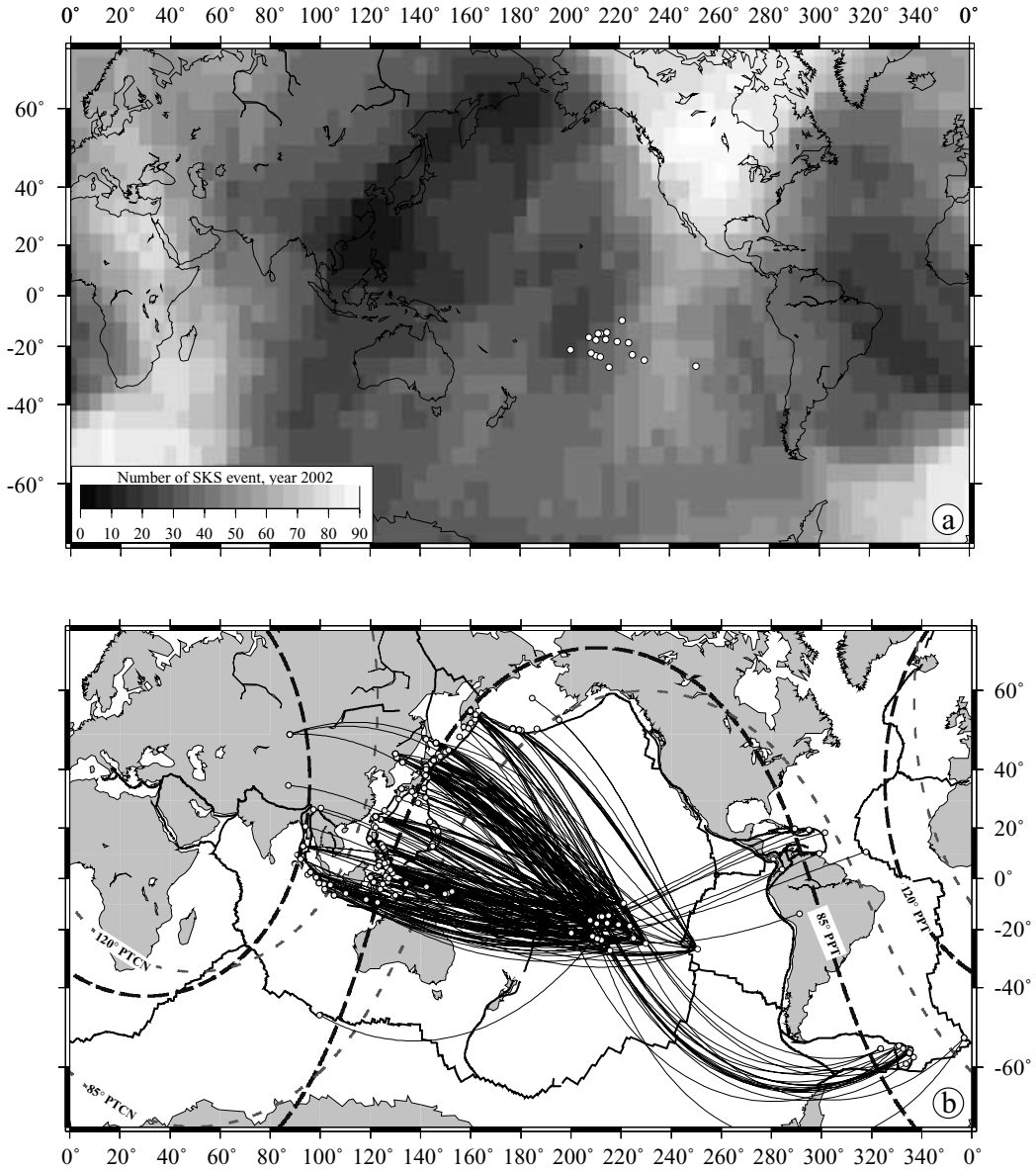

Figure 2. (a) Global map showing the density of recordable events ($m_b > 6.0$) occurring at epicentral distances in the range 85–120° for the year 2002. White/dark colours represent areas with a large/small number of observable SKS events. French Polynesia lies in a rather unfavourable situation with about 30 potentially usable events per year. (b) Location of the events that contributed to the 300 splitting measurements of this study, 60 of which being 'non-null' events. Great circles represent the 85° and 120° epicentral distances from stations PPT (thick dashed lines) and PTCN (thin dashed lines) to better visualize the location of the seismic sources that can potentially be used for SKS splitting studies in the South Pacific area.

that provides a pair of anisotropy parameters for each event and (ii) the multi-event analysis developed by Wolfe & Silver (1998) that calculates a pair of average anisotropy parameters for a set of several events.

The single event shear wave splitting method of Silver & Chan (1991) determines from a grid search the splitting parameters, Φ and δt, that best minimize energy on the transverse component of the seismogram for a selected time window. We mainly used the SKS phase, but for some events occurring at large enough distance, we perform both SKS and SKKS splitting measurements for the same event. The data from permanent and portable seismometers were systematically investigated. This allowed performing more than 300 individual splitting measurements, 60 of which are non-null, that is, display clear splitting (reported in Table 2). For each event, the corresponding splitting parameters (Φ, δt) are listed in Tables 2 and 3 with their 2σ uncertainty, determined from the 95 per cent confidence interval, the split phase on which we performed the measurement, and the backazimuth of the event. We also ascribe a quality factor (good, fair or poor) to the measurements depending on the signal-to-noise ratio of the initial phase, the rectilinear polarization of the horizontal particle motion after anisotropy correction, and the correlation between the fast and slow split shear waves as proposed by Barruol *et al.* (1997).

The multi event shear wave splitting measurement technique (Wolfe & Silver 1998) was initially developed to analyse noisy oceanic records (e.g. Russo & Okal 1998). It simultaneously combines several individual splitting measurements at a given station by stacking and normalizing the contour plot of the energy on the corrected transverse component. This method determines the best pair of Φ and δt that may explain the various waveforms. Such an

Table 2. Summary of the non-null splitting measurements performed at the permanent and at the PLUME temporary stations.

Station	Year	Month	Day	Time	Latitude (°)	Longitude (°)	Depth (km)	Phase	Backaz (°)	Φ (°)	σ_Φ	δt (s)	$\sigma_{\delta t}$	Qual
PTCN	2000	01	28	14:21:07.30	43.046	146.837	61	SKS	312	−69	13	1.60	0.50	g
PTCN	2002	11	17	04:53:53.50	47.824	146.209	459	SKS	316	85	6	0.84	0.10	g
PTCN	2003	06	16	22:08:02.10	55.492	159.999	174	SKS	327	83	7	1.16	0.25	g
PTCN	2004	06	10	15:19:57.70	55.682	160.003	188	SKS	327	−71	7	1.10	0.15	g
PTCN	2004	07	25	14:35:19.00	−2.427	103.981	582	SKKS	251	−47	12	1.60	0.45	f
RAR	1995	11	08	07:14:18.50	1.853	95.062	33	SKS	266	−71	14	1.76	0.64	f
RAR	1996	02	03	11:14:19.80	27.299	100.341	10	SKS	293	−50	7	1.74	0.40	f
RAR	2000	10	25	09:32:23.90	−6.549	105.630	38	SKS	262	−43	10	2.20	0.50	p
RAR	2002	11	02	01:26:10.70	2.824	96.085	30	SKS	268	−83	6	2.60	0.72	g
RAR	2004	07	25	14:35:19.00	−2.427	103.981	582	SKS	265	−30	17	1.05	0.41	f
RPN	1991	02	21	02:35:34.10	58.427	−175.450	20	SKS	331	47	6	1.80	0.48	f
RPN	1993	10	11	15:54:21.20	32.020	137.832	351	SKS	292	−22	12	0.85	0.20	f
RPN	1995	01	06	22:37:37.90	40.227	142.242	57	SKS	303	16	8	1.80	0.45	g
RPN	1997	12	05	11:26:54.60	54.841	162.035	33	SKS	322	40	8	2.60	0.75	p
RPN	2002	11	17	04:53:53.50	47.824	146.209	459	SKS	312	32	2	2.10	0.42	f
RPN	2003	06	15	19:24:33.10	51.552	176.923	20	SKS	322	43	7	2.50	0.76	p
RPN	2003	06	23	12:12:34.40	51.439	176.783	20	SKS	322	41	19	1.88	0.90	p
RKT	1995	12	25	04:43:24.90	−6.943	129.179	150	SKKS	261	−53	13	1.25	0.28	g
RKT	1996	01	01	08:05:11.90	0.724	119.981	33	SKS	265	−74	10	1.45	0.35	g
RKT	1996	07	22	14:19:35.70	1.000	120.450	33	SKKS	265	−71	12	2.10	0.70	p
RKT	2001	01	02	07:30:03.70	6.749	126.809	33	SKS	273	−52	20	1.30	1.00	f
RKT	2001	02	24	07:23:48.70	1.271	126.249	35	SKS	268	−52	10	1.20	0.30	g
RKT	2002	01	01	11:29:22.70	6.303	125.650	38	SKS	272	−71	10	2.15	0.75	f
RKT	2004	06	10	15:19:57.70	55.682	160.003	188	SKS	329	−41	4	1.55	0.38	g
RKT	2004	07	25	14:35:19.00	−2.427	103.981	582	SKS	254	−67	18	0.70	0.40	g
RKT	2004	07	25	14:35:19.00	−2.427	103.981	582	SKKS	254	−56	11	1.05	0.17	g
RKT	2005	03	02	10:42:12.20	−6.527	129.933	201	SKS	262	−42	20	1.35	0.80	g
TBI	1994	11	15	20:18:11.20	−5.606	110.201	559	SKS	261	87	2	2.90	0.63	p
TBI	1995	01	06	22:37:37.90	40.227	142.242	57	SKS	315	−64	6	1.80	0.58	f
TBI	2001	08	13	20:11:23.40	41.046	142.308	38	SKS	315	−57	8	2.10	0.80	f
TBI	2002	03	09	12:27:11.20	−56.019	−27.332	118	SKS	152	−53	11	1.95	0.67	f
TBI	2003	06	16	22:08:02.10	55.492	159.999	174	SKS	334	87	12	0.90	0.23	g
TBI	2004	07	25	14:35:19.00	−2.427	103.981	582	SKS	261	−84	13	1.10	0.40	f
TBI	2004	11	28	18:32:14.10	43.006	145.119	39	SKS	318	83	13	0.70	0.25	g
TPT	1990	05	12	04:50:08.70	49.037	141.847	605	SKS	322	−56	3	2.70	0.40	g
ANA	2003	05	26	23:13:29.70	6.761	123.707	565	SKS	276	−53	5	1.23	0.19	g
ANA	2004	06	10	15:19:57.70	55.682	160.003	188	SKS	333	−46	4	1.98	0.46	f
ANA	2004	07	25	14:35:19.00	−2.427	103.981	582	SKS	261	−49	20	0.88	0.54	f
ANA	2004	07	25	14:35:19.00	−2.427	103.981	582	SKKS	261	−75	8	1.33	0.29	g
HAO	2003	05	26	23:13:29.70	6.761	123.707	565	SKS	275	−63	6	1.80	0.38	g
HAO	2003	06	16	22:08:02.10	55.492	159.999	174	SKS	331	−81	14	0.85	0.24	g
HAO	2004	06	10	15:19:57.70	55.682	160.003	188	SKS	331	84	4	1.13	0.15	g
HAO	2004	07	25	14:35:19.00	−2.427	103.981	582	SKS	259	−53	6	1.55	0.19	g
HAO	2004	11	28	18:32:14.10	43.006	145.119	39	SKS	315	−58	6	1.93	0.60	f
HAO	2005	02	05	12:23:18.90	5.293	123.337	525	SKS	273	−55	3	1.30	0.11	g
HAO	2005	02	15	14:42:25.80	4.756	126.421	39	SKS	274	−37	14	1.33	0.49	f
HIV	2005	02	05	12:23:18.90	5.293	123.337	525	SKS	274	74	18	1.13	0.69	f
MA2	2002	11	17	04:53:53.50	47.824	146.209	459	SKS	323	72	5	1.27	0.33	p
MAT	2002	09	15	08:39:32.70	44.833	129.923	586	SKS	315	−67	10	1.88	0.49	f
RAI	2004	07	25	14:35:19.00	−2.427	103.981	582	SKS	260	−88	9	1.68	0.59	f
RAI	2004	07	25	14:35:19.00	−2.427	103.981	582	SKKS	260	−53	8	1.38	0.24	g
RAP	2003	06	16	22:08:02.10	55.492	159.999	174	SKS	332	−53	18	1.25	0.59	f
RAP	2003	09	25	19:50:06.30	41.815	143.910	27	SKS	314	−69	10	1.40	0.39	f
REA	2002	11	17	04:53:53.50	47.824	146.209	459	SKS	319	74	6	1.35	0.23	g
REA	2003	06	16	22:08:02.10	55.492	159.999	174	SKS	329	78	3	2.00	0.27	g
REA	2004	07	25	14:35:19.00	−2.427	103.981	582	SKS	257	−89	4	1.90	0.44	p
REA	2004	07	25	14:35:19.00	−2.427	103.981	582	SKKS	257	−64	6	1.25	0.17	g
REA	2005	03	02	10:42:12.20	−6.527	129.933	201	SKKS	263	−88	8	2.50	0.88	p
RUR	2003	06	16	22:08:02.10	55.492	159.999	174	SKS	335	−62	11	1.05	0.24	f
TAK	2002	11	02	01:26:10.70	2.824	96.085	30	SKS	265	−41	11	1.20	0.29	f
TAK	2002	11	17	04:53:53.50	47.824	146.209	459	SKS	321	64	9	1.48	0.50	g
TAK	2003	05	26	23:13:29.70	6.761	123.707	565	SKS	276	−75	4	2.15	0.56	f

Notes: Presented are the event information (date, time, location, backazimuth) and the corresponding splitting parameters, together with the 95 per cent confidence error and the overall quality of the measurement (g = good, f = fair, p = poor), as defined in the text.

Table 3. Summary of all (null and non-null) splitting measurements performed at the permanent and at the PLUME temporary sites.

Station	Year	Month	Day	Time	Lat (°)	Long (°)	Depth (km)	Phase	Backaz (°)	Φ (°)	δt (s)	Qual
PTCN	1997	03	26	02:08:57.20	51.277	179.533	33	SKS	331	Null	Null	– (R&O)
PTCN	1997	04	23	19:44:28.40	13.986	144.901	101	SKS	285	Null	Null	– (R&O)
PTCN	1997	12	05	18:48:22.70	53.752	161.746	33	SKS	326	Null	Null	p
PTCN	1998	06	01	05:34:03.50	52.889	160.067	44	SKS	325	Null	Null	p
PTCN	1998	09	02	08:37:29.90	5.410	126.764	50	SKS	269	Null	Null	p
PTCN	1999	12	11	18:03:36.40	15.766	119.740	33	SKS	277	Null	Null	p
PTCN	2000	01	28	14:21:07.30	43.046	146.837	61	SKS	312	-69 ± 13	1.6 ± 0.5	g
PTCN	2000	08	06	07:27:12.90	28.856	139.556	394	SKS	296	Null	Null	g
PTCN	2001	12	02	13:01:53.60	39.402	141.089	123	SKS	307	Null	Null	p
PTCN	2002	03	05	21:16:09.10	6.033	124.249	31	SKS	269	Null	Null	p
PTCN	2002	10	16	10:12:21.40	51.952	157.323	102	SKS	323	Null	Null	p
PTCN	2002	11	03	03:37:42.00	38.886	141.977	39	SKS	307	Null	Null	p
PTCN	2002	11	07	15:14:06.70	51.197	179.334	33	SKS	331	Null	Null	p
PTCN	2002	11	17	04:53:53.50	47.824	146.209	459	SKS	316	85 ± 6	0.84 ± 0.1	g
PTCN	2003	05	26	09:24:33.40	38.849	141.568	68	SKS	306	Null	Null	p
PTCN	2003	06	15	19:24:33.10	51.552	176.923	20	SKS	330	Null	Null	p
PTCN	2003	06	16	22:08:02.10	55.492	159.999	174	SKS	327	83 ± 7.5	1.16 ± 0.25	g
PTCN	2003	10	31	01:06:28.20	37.812	142.619	10	SKS	306	Null	Null	p
PTCN	2004	06	10	15:19:57.70	55.682	160.003	188	SKS	327	-71 ± 7	1.10 ± 0.15	g
PTCN	2004	07	25	14:35:19.00	−2.427	103.981	582	SKKS	251	-47 ± 12	1.60 ± 0.45	f
PTCN	2005	02	05	12:23:18.90	5.293	123.337	525	SKS	267	Null	Null	f
PTCN	2005	02	15	14:42:25.80	4.756	126.421	39	SKS	268	Null	Null	f
PTCN	2005	03	02	10:42:12.20	−6.527	129.933	201	SKS	259	Null	Null	f
RAR	1995	10	06	18:09:45.90	−2.089	101.414	33	SKS	265	Null	Null	p
RAR	1995	11	08	07:14:18.50	1.853	95.062	33	SKS	266	-71 ± 14	1.76 ± 0.64	f
RAR	1996	02	03	11:14:19.80	27.299	100.341	10	SKS	293	-50 ± 7	1.74 ± 0.40	f
RAR	1996	06	02	02:52:09.50	10.797	−42.254	10	SKS	89	Null	Null	f
RAR	1997	11	08	10:02:52.60	35.069	87.325	33	SKS	299	Null	Null	p
RAR	1997	11	28	22:53:41.50	−13.740	−68.788	586	SKS	103	Null	Null	p
RAR	1997	12	11	07:56:28.80	3.929	−75.787	178	SKS	84	Null	Null	p
RAR	2000	06	07	21:46:55.90	26.856	97.238	33	SKS	292	Null	Null	p
RAR	2000	06	10	18:23:29.30	23.843	121.225	33	SKS	296	Null	Null	p
RAR	2000	10	25	09:32:23.90	−6.549	105.630	38	SKS	262	-43 ± 10	2.2 ± 0.5	p
RAR	2000	11	07	00:18:04.90	−55.627	−29.876	10	SKS	154	Null	Null	p
RAR	2001	10	17	11:29:09.90	19.354	−64.932	33	SKS	74	Null	Null	p
RAR	2002	06	28	17:19:30.20	43.752	130.666	566	SKS	317	Null	Null	p
RAR	2002	09	13	22:28:29.40	13.036	93.068	21	SKS	277	Null	Null	p
RAR	2002	09	15	08:39:32.70	44.833	129.923	586	SKS	318	Null	Null	p
RAR	2002	11	02	01:26:10.70	2.824	96.085	30	SKS	268	-83 ± 6	2.60 ± 0.72	g
RAR	2002	11	02	09:46:46.70	2.954	96.394	27	SKS	268	Null	Null	p
RAR	2003	09	22	04:45:36.20	19.777	−70.673	10	SKS	71	Null	Null	p
RAR	2003	09	27	11:33:25.00	50.038	87.813	16	SKS	316	Null	Null	p
RAR	2004	07	25	14:35:19.00	−2.427	103.981	582	SKS	265	-30 ± 17.5	1.05 ± 0.41	f
RPN	1991	02	21	02:35:34.10	58.427	−175.450	20	SKS	331	47 ± 6.5	1.8 ± 0.48	f
RPN	1993	04	19	21:01:48.90	4.015	128.204	23	SKS	258	Null	Null	p
RPN	1993	08	08	08:34:24.90	12.982	144.801	59	SKS	275	Null	Null	p
RPN	1993	10	11	15:54:21.20	32.020	137.832	351	SKS	292	-22 ± 12	0.85 ± 0.2	f
RPN	1995	01	06	22:37:37.90	40.227	142.242	57	SKS	303	16 ± 8	1.8 ± 0.45	g
RPN	1997	12	05	11:26:54.60	54.841	162.035	33	SKS	322	40 ± 8	2.6 ± 0.75	p
RPN	1998	11	29	14:10:31.90	−2.071	124.891	33	SKS	250	Null	Null	p
RPN	2000	02	06	11:33:52.20	−5.844	150.876	33	SKS	260	Null	Null	p
RPN	2000	03	28	11:00:22.50	22.338	143.730	126	SKS	284	Null	Null	p
RPN	2000	06	09	01:27:15.10	−5.071	152.495	33	SKS	262	Null	Null	p
RPN	2001	02	24	07:23:48.70	1.271	126.249	35	SKKS	254	Null	Null	p
RPN	2001	06	14	19:48:47.80	51.160	−179.828	18	SKS	323	Null	Null	f
RPN	2001	06	15	06:17:45.30	18.833	146.983	33	SKS	281	Null	Null	p
RPN	2001	12	02	13:01:53.60	39.402	141.089	123	SKS	301	Null	Null	p
RPN	2002	01	10	11:14:56.90	−3.212	142.427	11	SKS	259	Null	Null	p
RPN	2002	11	07	15:14:06.70	51.197	179.334	33	SKS	323	Null	Null	p
RPN	2002	11	17	04:53:53.50	47.824	146.209	459	SKS	312	32 ± 2	2.10 ± 0.42	f
RPN	2002	11	26	00:48:15.00	51.465	−173.537	20	SKS	326	Null	Null	p
RPN	2003	02	10	04:49:31.10	−6.011	149.792	33	SKS	260	Null	Null	p
RPN	2003	02	19	03:32:36.30	53.645	−164.643	19	SKS	331	Null	Null	p

Table 3. (*Continued.*)

Station	Year	Month	Day	Time	Lat (°)	Long (°)	Depth (km)	Phase	Backaz (°)	Φ (°)	δt (s)	Qual
RPN	2003	06	15	19:24:33.10	51.552	176.923	20	SKS	322	43 ± 7	2.50 ± 0.76	p
RPN	2003	06	16	22:08:02.10	55.492	159.999	174	SKS	322	Null	Null	p
RPN	2003	06	23	12:12:34.40	51.439	176.783	20	SKS	322	41 ± 19	1.88 ± 0.90	p
RAI	2003	05	26	09:24:33.40	38.849	141.568	68	SKS	313	Null	Null	p
RAI	2003	05	26	23:13:29.70	6.761	123.707	565	SKKS	277	Null	Null	f
RAI	2003	06	16	22:08:02.10	55.492	159.999	174	SKS	333	Null	Null	f
RAI	2003	09	25	19:50:06.30	41.815	143.910	27	SKS	316	Null	Null	f
RAI	2004	06	10	15:19:57.70	55.682	160.003	188	SKS	333	Null	Null	g
RAI	2004	07	25	14:35:19.00	−2.427	103.981	582	SKS	260	−88 ± 9.5	1.68 ± 0.59	f
RAI	2004	07	25	14:35:19.00	−2.427	103.981	582	SKKS	260	−53 ± 8	1.38 ± 0.24	g
ANA	2002	03	31	06:52:50.40	24.279	122.179	32	SKS	293	Null	Null	f
ANA	2002	06	13	01:27:19.40	−47.801	99.751	10	SKS	218	Null	Null	p
ANA	2002	09	13	22:28:29.40	13.036	93.068	21	SKKS	274	Null	Null	f
ANA	2002	10	14	14:12:43.70	41.174	142.249	61	SKS	314	Null	Null	f
ANA	2002	11	02	01:26:10.70	2.824	96.085	30	SKS	264	Null	Null	g
ANA	2002	11	02	09:46:46.70	2.954	96.394	27	SKS	264	Null	Null	f
ANA	2002	11	03	03:37:42.00	38.886	141.977	39	SKS	312	Null	Null	f
ANA	2002	11	17	04:53:53.50	47.824	146.209	459	SKS	321	Null	Null	g
ANA	2002	12	17	04:32:53.00	−56.952	−24.825	10	SKS	152	Null	Null	g
ANA	2002	12	18	14:12:21.70	−57.092	−24.981	10	SKS	152	Null	Null	p
ANA	2003	01	06	23:43:50.80	15.651	119.658	10	SKS	284	Null	Null	g
ANA	2003	05	26	23:13:29.70	6.761	123.707	565	SKS	276	−53 ± 5.5	1.23 ± 0.19	g
ANA	2003	10	31	01:06:28.20	37.812	142.619	10	SKS	311	Null	Null	f
ANA	2004	06	10	15:19:57.70	55.682	160.003	188	SKS	333	−46 ± 4	1.98 ± 0.46	f
ANA	2004	07	25	14:35:19.00	−2.427	103.981	582	SKS	261	−49 ± 20.5	0.88 ± 0.54	f
ANA	2004	07	25	14:35:19.00	−2.427	103.981	582	SKKS	261	−75 ± 8	1.33 ± 0.29	g
ANA	2004	11	08	15:55:01.10	24.104	122.542	29	SKS	293	Null	Null	g
ANA	2004	11	28	18:32:14.10	43.006	145.119	39	SKS	317	Null	Null	g
HAO	2001	10	19	03:28:44.40	−4.102	123.907	33	SKS	265	Null	Null	f
HAO	2002	03	05	21:16:09.10	6.033	124.249	31	SKS	274	Null	Null	g
HAO	2002	03	26	03:45:48.70	23.346	124.090	33	SKS	291	Null	Null	p
HAO	2002	03	31	06:52:50.40	24.279	122.179	32	SKS	291	Null	Null	g
HAO	2003	05	26	09:24:33.40	38.849	141.568	68	SKS	310	Null	Null	f
HAO	2003	05	26	19:23:27.90	2.354	128.855	31	SKS	272	Null	Null	g
HAO	2003	05	26	23:13:29.70	6.761	123.707	565	SKS	275	−63 ± 6	1.8 ± 0.38	g
HAO	2003	06	16	22:08:02.10	55.492	159.999	174	SKS	331	−81 ± 14	0.85 ± 0.24	g
HAO	2003	09	29	02:36:53.10	42.450	144.380	25	SKS	314	Null	Null	p
HAO	2003	10	08	09:06:55.30	42.648	144.570	32	SKS	315	Null	Null	p
HAO	2003	10	18	22:27:13.20	0.444	126.103	33	SKS	270	Null	Null	p
HAO	2003	10	31	01:06:28.20	37.812	142.619	10	SKS	310	Null	Null	p
HAO	2003	11	18	17:14:22.60	12.025	125.416	35	SKS	280	Null	Null	p
HAO	2004	05	29	20:56:09.60	34.251	141.406	16	SKS	306	Null	Null	p
HAO	2004	06	10	15:19:57.70	55.682	160.003	188	SKS	331	84 ± 4	1.13 ± 0.15	g
HAO	2004	07	25	14:35:19.00	−2.427	103.981	582	SKS	259	−53 ± 6	1.55 ± 0.19	g
HAO	2004	09	06	23:29:35.00	33.205	137.227	10	SKS	304	Null	Null	p
HAO	2004	11	28	18:32:14.10	43.006	145.119	39	SKS	315	−58 ± 6	1.93 ± 0.6	f
HAO	2004	12	06	14:15:11.80	42.900	145.228	35	SKS	315	Null	Null	p
HAO	2005	02	05	12:23:18.90	5.293	123.337	525	SKS	273	−55 ± 3	1.30 ± 0.11	g
HAO	2005	02	15	14:42:25.80	4.756	126.421	39	SKS	274	−37 ± 14.5	1.33 ± 0.49	f
HIV	2001	10	19	03:28:44.40	−4.102	123.907	33	SKS	265	Null	Null	f
HIV	2001	12	02	13:01:53.60	39.402	141.089	123	SKS	310	Null	Null	f
HIV	2001	12	18	04:02:58.20	23.954	122.734	14	SKS	293	Null	Null	f
HIV	2002	01	01	11:29:22.70	6.303	125.650	138	SKS	275	Null	Null	f
HIV	2002	03	05	21:16:09.10	6.033	124.249	31	SKS	275	Null	Null	f
HIV	2002	03	26	03:45:48.70	23.346	124.090	33	SKS	292	Null	Null	f
HIV	2002	03	31	06:52:50.40	24.279	122.179	32	SKS	293	Null	Null	f
HIV	2002	07	30	06:55:07.70	−57.889	−23.242	33	SKS	151	Null	Null	p
HIV	2002	08	02	23:11:39.10	29.280	138.970	426	SKS	300	Null	Null	f
HIV	2002	08	15	05:30:26.20	−1.196	121.333	10	SKS	267	Null	Null	f
HIV	2002	08	24	18:40:53.40	43.110	146.118	42	SKS	315	Null	Null	p
HIV	2002	09	13	22:28:29.40	13.036	93.068	21	SKKS	279	Null	Null	p
HIV	2002	09	13	22:28:29.40	13.036	93.068	21	SKS	279	Null	Null	f
HIV	2002	09	15	08:39:32.70	44.833	129.923	586	SKS	314	Null	Null	g

Table 3. (*Continued.*)

Station	Year	Month	Day	Time	Lat (°)	Long (°)	Depth (km)	Phase	Backaz (°)	Φ (°)	δt (s)	Qual
HIV	2002	10	10	10:50:20.50	−1.757	134.297	10	SKS	269	Null	Null	f
HIV	2002	10	14	14:12:43.70	41.174	142.249	61	SKS	312	Null	Null	f
HIV	2002	11	02	01:26:10.70	2.824	96.085	30	PKS	267	Null	Null	f
HIV	2002	11	03	03:37:42.00	38.886	141.977	39	SKS	310	Null	Null	g
HIV	2002	11	17	04:53:53.50	47.824	146.209	459	SKS	319	Null	Null	g
HIV	2003	05	05	15:50:08.40	0.215	127.354	123	SKS	270	Null	Null	g
HIV	2003	05	11	17:51:35.10	−0.988	126.938	30	SKS	268	Null	Null	p
HIV	2004	05	29	20:56:09.60	34.251	141.406	16	SKS	305	Null	Null	f
HIV	2004	07	25	14:35:19.00	−2.427	103.981	582	SKS	263	Null	Null	p
HIV	2004	07	25	14:35:19.00	−2.427	103.981	582	SKKS	263	Null	Null	f
HIV	2004	09	05	10:07:07.80	33.070	136.618	14	SKS	303	Null	Null	f
HIV	2004	09	06	12:42:59.30	−55.372	−28.976	10	SKS	148	Null	Null	g
HIV	2004	10	26	22:53:07.80	−57.071	−24.679	10	SKS	150	Null	Null	g
HIV	2004	11	28	18:32:14.10	43.006	145.119	39	SKS	315	Null	Null	g
HIV	2004	12	06	14:15:11.80	42.900	145.228	35	SKS	315	Null	Null	g
HIV	2005	02	05	12:23:18.90	5.293	123.337	525	SKS	274	74 ± 18	1.13 ± 0.69	f
MAU	2002	06	22	02:58:21.30	35.626	49.047	10	SKSdf	319	Null	Null	p
MA2	2002	11	15	19:58:31.70	−56.051	−36.404	10	SKS	150	Null	Null	p
MA2	2002	11	17	04:53:53.50	47.824	146.209	459	SKS	323	72 ± 5	1.27 ± 0.33	p
MA2	2003	09	22	04:45:36.20	19.777	−70.673	10	SKS	69	Null	Null	f
MA2	2004	07	25	14:35:19.00	−2.427	103.981	582	SKS	264	Null	Null	g
MA2	2004	07	25	14:35:19.00	−2.427	103.981	582	SKKS	264	Null	Null	g
MA2	2004	09	06	12:42:59.30	−55.372	−28.976	10	SKS	151	Null	Null	f
MA2	2004	11	08	15:55:01.10	24.104	122.542	29	SKS	294	Null	Null	f
MAT	2002	03	05	21:16:09.10	6.033	124.249	31	SKS	277	Null	Null	f
MAT	2002	03	26	03:45:48.70	23.346	124.090	33	SKS	293	Null	Null	p
MAT	2002	03	31	06:52:50.40	24.279	122.179	32	SKS	294	Null	Null	f
MAT	2002	05	28	16:45:17.10	24.069	122.264	33	SKS	293	Null	Null	p
MAT	2002	09	13	22:28:29.40	13.036	93.068	21	SKS	277	Null	Null	p
MAT	2002	09	15	08:39:32.70	44.833	129.923	586	SKS	315	−67 ± 10	1.88 ± 0.49	f
MAT	2002	11	15	19:58:31.70	−56.051	−36.404	10	SKS	149	Null	Null	p
MAT	2002	11	17	04:53:53.50	47.824	146.209	459	SKS	322	Null	Null	p
MAT	2003	05	26	23:13:29.70	6.761	123.707	565	SKS	277	Null	Null	f
MAT	2003	09	27	11:33:25.00	50.038	87.813	16	SKKS	320	Null	Null	f
MAT	2004	07	25	14:35:19.00	−2.427	103.981	582	SKS	263	Null	Null	p
MAT	2004	09	06	12:42:59.30	−55.372	−28.976	10	SKS	150	Null	Null	g
RAP	2001	12	02	13:01:53.60	39.402	141.089	123	SKS	311	Null	Null	f
RAP	2002	03	05	21:16:09.10	6.033	124.249	31	SKS	275	Null	Null	f
RAP	2002	03	31	06:52:50.40	24.279	122.179	32	SKS	290	Null	Null	p
RAP	2002	05	28	16:45:17.10	24.069	122.264	33	SKS	290	Null	Null	f
RAP	2002	07	11	07:36:26.00	24.075	122.288	43	SKS	290	Null	Null	f
RAP	2002	10	06	15:46:33.00	−8.197	118.341	10	SKS	259	Null	Null	f
RAP	2003	05	26	09:24:33.40	38.849	141.568	68	SKS	311	Null	Null	p
RAP	2003	05	26	23:13:29.70	6.761	123.707	565	SKS	275	Null	Null	g
RAP	2003	06	16	22:08:02.10	55.492	159.999	174	SKS	332	−53 ± 18	1.25 ± 0.59	f
RAP	2003	09	25	19:50:06.30	41.815	143.910	27	SKS	314	−69 ± 10	1.40 ± 0.39	f
RAP	2003	10	31	01:06:28.20	37.812	142.619	10	SKS	311	Null	Null	p
RAP	2003	11	01	13:10:07.60	37.742	143.083	10	SKS	311	Null	Null	f
REA	2002	03	31	06:52:50.40	24.279	122.179	32	SKS	290	Null	Null	f
REA	2002	08	20	10:59:32.00	30.986	141.966	9	SKS	302	Null	Null	p
REA	2002	10	14	14:12:43.70	41.174	142.249	61	SKS	311	Null	Null	f
REA	2002	11	17	04:53:53.50	47.824	146.209	459	SKS	319	74 ± 6	1.35 ± 0.23	g
REA	2003	05	26	09:24:33.40	38.849	141.568	68	SKS	309	Null	Null	p
REA	2003	05	26	19:23:27.90	2.354	128.855	31	SKS	271	Null	Null	f
REA	2003	05	26	23:13:29.70	6.761	123.707	565	SKS	273	Null	Null	p
REA	2003	06	16	22:08:02.10	55.492	159.999	174	SKS	329	78 ± 3	2 ± 0.27	g
REA	2003	11	18	17:14:22.60	12.025	125.416	35	SKS	279	Null	Null	p
REA	2004	07	25	14:35:19.00	−2.427	103.981	582	SKS	257	−89 ± 4	1.9 ± 0.44	p
REA	2004	07	25	14:35:19.00	−2.427	103.981	582	SKKS	257	−64 ± 6	1.25 ± 0.17	g
REA	2004	09	05	10:07:07.80	33.070	136.618	14	SKS	302	Null	Null	f
REA	2004	11	28	18:32:14.10	43.006	145.119	39	SKS	314	Null	Null	f
REA	2004	12	06	14:15:11.80	42.900	145.228	35	SKS	314	Null	Null	p
REA	2005	02	05	12:23:18.90	5.293	123.337	525	SKS	272	Null	Null	g

Table 3. (*Continued.*)

Station	Year	Month	Day	Time	Lat (°)	Long (°)	Depth (km)	Phase	Backaz (°)	Φ (°)	δt (s)	Qual
REA	2005	02	15	14:42:25.80	4.756	126.421	39	SKS	272	Null	Null	p
REA	2005	03	02	10:42:12.20	−6.527	129.933	201	SKKS	263	−88 ± 8	2.5 ± 0.88	p
RUR	2002	03	31	06:52:50.40	24.279	122.179	32	SKS	294	Null	Null	f
RUR	2002	10	14	14:12:43.70	41.174	142.249	61	SKS	316	Null	Null	g
RUR	2002	10	16	10:12:21.40	51.952	157.323	102	SKS	331	Null	Null	p
RUR	2002	11	02	01:26:10.70	2.824	96.085	30	SKS	264	Null	Null	g
RUR	2002	11	03	03:37:42.00	38.886	141.977	39	SKS	314	Null	Null	f
RUR	2003	05	26	23:13:29.70	6.761	123.707	565	SKS	278	Null	Null	f
RUR	2003	06	16	22:08:02.10	55.492	159.999	174	SKS	335	−62 ± 11	1.05 ± 0.24	f
TAK	2002	03	05	21:16:09.10	6.033	124.249	31	SKS	276	Null	Null	p
TAK	2002	03	26	03:45:48.70	23.346	124.090	33	SKS	292	Null	Null	p
TAK	2002	03	31	06:52:50.40	24.279	122.179	32	SKS	293	Null	Null	g
TAK	2002	05	28	16:45:17.10	24.069	122.264	33	SKS	293	Null	Null	p
TAK	2002	09	13	22:28:29.40	13.036	93.068	21	SKS	276	Null	Null	p
TAK	2002	09	15	08:39:32.70	44.833	129.923	586	SKS	315	Null	Null	f
TAK	2002	11	02	01:26:10.70	2.824	96.085	30	SKSdf	265	−41 ± 11	1.2 ± 0.29	f
TAK	2002	11	17	04:53:53.50	47.824	146.209	459	SKS	321	64 ± 9.5	1.48 ± 0.50	g
TAK	2003	05	14	06:03:35.80	18.266	−58.633	41	SKS	272	Null	Null	p
TAK	2003	05	26	23:13:29.70	6.761	123.707	565	SKS	276	−75 ± 4	2.15 ± 0.56	f
TAK	2003	07	01	05:52:25.90	4.529	122.511	635	SKS	274	Null	Null	p
TAK	2003	09	27	11:33:25.00	50.038	87.813	16	SKKS	321	Null	Null	f
TAK	2003	10	18	22:27:13.20	0.444	126.103	33	SKS	271	Null	Null	p
TAOE	2005	03	02	10:42:12.20	−6.527	129.933	201	SKS	264	Null	Null	f
RKTL	1995	12	25	04:43:24.90	−6.943	129.179	150	SKKS	261	−53 ± 13	1.25 ± 0.28	g
RKTL	1996	01	01	08:05:11.90	0.724	119.981	33	SKS	265	−74 ± 10	1.45 ± 0.35	g
RKTL	1996	02	07	21:36:45.10	45.321	149.902	33	SKS	317	Null	Null	− (R&O)
RKTL	1996	06	21	13:57:10.00	51.568	159.119	20	SKS	325	Null	Null	− (R&O)
RKTL	1996	07	22	14:19:35.70	1.000	120.450	33	SKKS	265	−71 ± 12	2.10 ± 0.70	p
RKTL	1996	10	18	10:50:20.80	30.568	131.290	10	SKS	297	Null	Null	− (R&O)
RKTL	2000	07	25	03:14:29.70	−53.553	−3.169	10	SKS	154	Null	Null	p
RKTL	2000	12	22	10:13:01.10	44.790	147.196	140	SKS	315	Null	Null	f
RKTL	2001	01	01	06:57:04.10	6.898	126.579	33	SKS	273	Null	Null	p
RKTL	2001	01	02	07:30:03.70	6.749	126.809	33	SKS	273	−52 ± 20	1.3 ± 1	f
RKTL	2001	02	24	07:23:48.70	1.271	126.249	35	SKS	268	−52 ± 10	1.2 ± 0.3	g
RKTL	2001	10	19	03:28:44.40	−4.102	123.907	33	SKS	262	Null	Null	f
RKTL	2002	01	01	11:29:22.70	6.303	125.650	38	SKS	272	−71 ± 10	2.15 ± 0.75	f
RKTL	2002	01	28	13:50:28.70	49.381	155.594	33	SKS	322	Null	Null	p
RKTL	2002	03	26	03:45:48.70	23.346	124.090	33	SKS	288	Null	Null	p
RKTL	2003	05	05	15:50:08.40	0.215	127.354	123	SKS	267	Null	Null	p
RKTL	2003	05	05	23:04:45.60	3.715	127.954	56	SKS	271	Null	Null	p
RKTL	2004	04	23	01:50:30.20	−9.362	122.839	65	SKS	257	Null	Null	f
RKTL	2004	05	29	20:56:09.60	34.251	141.406	16	SKS	304	Null	Null	f
RKTL	2004	06	10	15:19:57.70	55.682	160.003	188	SKS	329	−41 ± 4	1.55 ± 0.38	g
RKTL	2004	07	25	14:35:19.00	−2.427	103.981	582	SKS	254	−67 ± 18	0.7 ± 0.4	g
RKTL	2004	07	25	14:35:19.00	−2.427	103.981	582	SKKS	254	−56 ± 11	1.05 ± 0.17	g
RKTL	2004	11	28	18:32:14.10	43.006	145.119	39	SKS	313	Null	Null	g
RKTL	2004	11	28	18:32:14.10	43.006	145.119	39	SKKS	313	Null	Null	g
RKTL	2004	12	06	14:15:11.80	42.900	145.228	35	SKS	313	Null	Null	g
RKTL	2004	12	06	14:15:11.80	42.900	145.228	35	SKKS	313	Null	Null	g
RKTL	2005	03	02	10:42:12.20	−6.527	129.933	201	SKS	262	−42 ± 20	1.35 ± 0.80	g
RKTL	2005	04	10	10:29:11.20	−1.644	99.607	19	SKKS	253	Null	Null	f
RKTL	2005	07	24	15:42:06.20	7.920	92.190	16	SKS	259	Null	Null	p
RKTL	2005	08	16	02:46:28.30	38.252	142.077	36	SKS	308	Null	Null	g
TBI	1993	12	10	08:59:35.80	20.912	121.282	12	SKS	289	Null	Null	− (R&O)
TBI	1994	05	03	16:36:43.60	10.241	−60.758	36	SKS	80	Null	Null	p
TBI	1994	05	23	05:36:01.60	24.166	122.535	20	SKS	293	Null	Null	p
TBI	1994	05	29	14:11:50.90	20.556	94.160	36	SKS	281	Null	Null	− (R&O)
TBI	1994	11	14	19:15:30.70	13.532	121.087	33	SKS	283	Null	Null	− (R&O)
TBI	1994	11	15	20:18:11.20	−5.606	110.201	559	SKS	261	87 ± 2	2.9 ± 0.63	p
TBI	1995	01	06	22:37:37.90	40.227	142.242	57	SKS	315	−64 ± 6	1.8 ± 0.58	f
TBI	1995	04	17	23:28:08.30	45.904	151.288	34	SKS	323	Null	Null	p
TBI	1995	04	21	00:09:56.20	11.999	125.699	33	SKS	283	Null	Null	− (R&O)
TBI	1995	05	05	03:53:47.60	12.622	125.314	33	SKS	283	Null	Null	− (R&O)

Table 3. (*Continued.*)

Station	Year	Month	Day	Time	Lat (°)	Long (°)	Depth (km)	Phase	Backaz (°)	Φ (°)	δt (s)	Qual
TBI	1996	06	11	18:22:55.70	12.614	125.154	33	SKS	283	Null	Null	– (R&O)
TBI	2000	01	06	21:31:06.20	16.095	119.484	33	SKS	284	Null	Null	f
TBI	2000	06	07	23:45:26.60	−4.612	101.905	33	SKS	258	Null	Null	p
TBI	2000	07	25	03:14:29.70	−53.553	−3.169	10	SKS	160	Null	Null	p
TBI	2000	10	25	09:32:23.90	−6.549	105.630	38	SKS	258	Null	Null	f
TBI	2001	01	03	14:47:49.50	43.932	147.813	33	SKS	320	Null	Null	f
TBI	2001	01	16	13:25:09.80	−4.022	101.776	28	SKS	259	Null	Null	f
TBI	2001	03	24	06:27:53.50	34.083	132.526	50	SKS	306	Null	Null	f
TBI	2001	08	13	20:11:23.40	41.046	142.308	38	SKS	315	-57 ± 8	2.1 ± 0.8	f
TBI	2002	03	09	12:27:11.20	−56.019	−27.332	118	SKS	152	-53 ± 11	1.95 ± 0.67	f
TBI	2003	05	26	09:24:33.40	38.849	141.568	68	SKS	313	Null	Null	g
TBI	2003	06	16	22:08:02.10	55.492	159.999	174	SKS	334	87 ± 12.5	0.90 ± 0.23	g
TBI	2003	10	31	01:06:28.20	37.812	142.619	10	SKS	313	Null	Null	g
TBI	2004	06	10	15:19:57.70	55.682	160.003	188	SKS	334	Null	Null	f
TBI	2004	07	25	14:35:19.00	−2.427	103.981	582	SKS	261	-84 ± 13	1.1 ± 0.4	f
TBI	2004	11	28	18:32:14.10	43.006	145.119	39	SKS	318	83 ± 13.5	0.70 ± 0.25	g
TBI	2004	12	06	14:15:11.80	42.900	145.228	35	SKS	318	Null	Null	p
TBI	2005	02	05	12:23:18.90	5.293	123.337	525	SKS	276	Null	Null	g
TBI	2005	04	10	10:29:11.20	−1.644	99.607	19	SKS	260	Null	Null	p
TBI	2005	05	14	05:05:18.40	0.587	98.459	34	SKS	262	Null	Null	f
TBI	2005	07	24	15:42:06.20	7.920	92.190	16	SKS	266	Null	Null	p
TBI	2005	08	16	02:46:28.30	38.252	142.077	36	SKS	313	Null	Null	g
TPTL	1990	05	12	04:50:08.70	49.037	141.847	605	SKS	322	-56 ± 3	2.7 ± 0.4	g (R&O)
TPTL	1993	05	02	11:26:54.90	−56.415	−24.491	12	SKS	152	Null	Null	p
TPTL	1994	05	24	04:00:42.10	23.959	122.448	16	SKS	293	Null	Null	p
TPTL	1994	06	05	01:09:30.10	24.511	121.905	11	SKS	294	Null	Null	p
TPTL	1994	07	21	18:36:31.70	42.301	132.892	473	SKS	313	-67 ± 22	1 ± 1.4	f
TPTL	1994	10	12	06:43:41.80	13.738	124.521	33	SKS	284	Null	Null	p
TPTL	1995	04	23	05:08:03.20	12.377	125.364	33	SKS	283	Null	Null	p
TPTL	1995	05	08	18:08:09.60	11.567	125.900	33	SKS	282	Null	Null	p
PPT	1990	05	12	04:50:08.70	49.037	141.847	605	SKS	322	Null	Null	g (R&O)
PPT	1991	12	27	04:05:58.20	−56.032	−25.266	10	SKS	153	Null	Null	g (B&H)
PPT	1991	12	28	00:52:10.20	−56.102	−24.614	10	SKS	153	Null	Null	p (B&H)
PPT	1993	01	10	14:39:00.40	−59.274	−26.205	61	SKS	155	Null	Null	f (B&H)
PPT	1993	05	02	11:26:54.90	−56.415	−24.491	12	SKS	152	Null	Null	– (R&O)
PPT	1993	08	07	00:00:37.00	26.585	125.612	155	SKS	297	Null	Null	– (R&O)
PPT	1994	07	21	18:36:31.70	42.301	132.892	473	SKS	313	Null	Null	– (R&O)
PPT	1994	09	28	16:39:52.20	−5.773	110.329	643	SKS	261	Null	Null	– (R&O)
PPT	1995	01	06	22:37:37.90	40.227	142.242	57	SKS	315	Null	Null	– (R&O)
PPT	1995	04	21	00:09:56.20	11.999	125.699	33	SKS	283	Null	Null	– (R&O)
PPT	1996	01	01	08:05:11.90	0.724	119.981	33	SKS	271	Null	Null	g (B&H)
PPT	1996	06	11	18:22:55.70	12.614	125.154	33	SKS	283	Null	Null	f (B&H)
PPT	1999	04	08	13:10:34.00	43.607	130.350	566	SKS	314	Null	Null	p
PPT	1999	12	11	18:03:36.40	15.766	119.740	33	SKS	285	Null	Null	p
PPT	2000	07	16	03:21:45.50	20.253	122.043	33	SKS	290	Null	Null	p
PPT	2000	08	04	21:13:02.70	48.786	142.246	10	SKS	322	Null	Null	p
PPT	2002	06	28	17:19:30.20	43.752	130.666	566	SKS	314	Null	Null	p
PPTL	1993	05	02	11:26:54.90	−56.415	−24.491	12	SKS	153	Null	Null	g
PPTL	1994	07	21	18:36:31.70	42.301	132.892	473	SKS	314	Null	Null	g
PPTL	2002	03	31	06:52:50.40	24.279	122.179	32	SKS	294	Null	Null	g
PPTL	2002	09	13	22:28:29.40	13.036	93.068	21	SKS	275	Null	Null	g
PPTL	2002	09	15	08:39:32.70	44.833	129.923	586	SKS	315	Null	Null	g
PPTL	2002	10	06	15:46:33.00	−8.197	118.341	10	SKKS	262	Null	Null	f
PPTL	2002	11	17	04:53:53.50	47.824	146.209	459	SKS	323	Null	Null	g
PPTL	2002	12	17	04:32:53.00	−56.952	−24.825	10	SKS	153	Null	Null	p
PPTL	2004	07	25	14:35:19.00	−2.427	103.981	582	SKS	263	Null	Null	g
PPTL	2005	02	05	12:23:18.90	5.293	123.337	525	SKS	276	Null	Null	g
PPTL	2005	05	14	05:05:18.40	0.587	98.459	34	SKS	264	Null	Null	p

Notes: Here we present the event information (date, time, location and backazimuth) and the anisotropy parameters. 'Null' measurements indicated events for which no anisotropy has been detected, that is, when no energy was present on the transverse component. Some individual measurements marked as R&O and B&H were already published by Russo & Okal (1998) and by Barruol & Hoffmann (1999), respectively. Lat and Long are latitude and longitude of the earthquake hypocenter. Backaz is the event backazimuth and Qual is the quality of the measurement.

approach can be useful at stations with only few data and/or on sets of data showing a weak but real energy on the transverse component, suggesting that the core shear wave has really been split. It is however important to keep in mind the limitation of this method which assumes a homogeneous structure beneath the station. This condition is probably fulfilled if no backazimuthal variation is visible from the individual splitting measurements or if one performs the measurements on groups of data arriving from similar backazimuths, that is, sampling roughly the same anisotropic region. In this case, the stacking method yields more robust splitting parameters and reduces the 95 per cent confidence regions compared to the analyses of individual events.

2.4 Effect of microseismic noise on shear wave splitting measurements

Seismic stations installed on oceanic islands or in coastal environments are generally subject to high noise level in the 1–20 s period, due to the oceanic wave activity (Peterson 1993; Stutzmann *et al.* 2000; Berger *et al.* 2004; McNamara & Buland 2004). The microseismic noise spectrum is generally characterized by a dominant peak centered around 5 s of period, called the 'double frequency peak' (hereafter called the DF peak), roughly centered on twice the swell dominant frequency (e.g. Bromirski & Duennebier 2002). This worldwide feature is attributed to non-linear interactions between waves travelling in opposite directions (Longuet-Higgins 1950), that might create standing waves in the ocean and elastic waves propagating in the ocean floor (Hasselmann 1963). At most oceanic stations, a less energetic peak is also visible on the microseismic noise spectra at periods in the range 10–20 s. This peak is particularly visible at the seismic stations running in French Polynesia (Barruol *et al.* 2006). This 'single frequency peak' (hereafter called the SF peak), which is more energetic on the horizontal than on the vertical components, is in the same period range as the swell and is classically attributed to the conversion of swell energy into elastic waves by the continuous regime of pressure variations applied on the external slopes of the island (Hasselmann 1963).

Since teleseismic shear waves are characterized by dominant periods around 10 s and by dominant ground motion in the horizontal plane, one has to be aware that part of the shear wave splitting signal could interact with part of the SF or DF microseismic noise, an effect that may be difficult to remove by frequency filtering (e.g. Hammond *et al.* 2005). Noise analyses on data from South Pacific temporary and permanent stations (Barruol *et al.* 2006) showed that the microseismic noise in the DF band is not polarized, that is, the ground motion in this band is randomly oriented. In the absence of anisotropy beneath the receiver this part of the noise would not provide a non-null splitting measurement. On the other hand, it has been shown by these authors that the swell-induced seismic noise in the SF band is elliptically polarized in the horizontal plane. In this band, the strength of the polarization (i.e. the degree of particle motion linearity) has been demonstrated to be strongly correlated to the swell height and the direction of the ground motion polarization to be controlled either by the swell propagation direction or by the island geometry. These findings suggest that an SKS phase arriving during a strong oceanic swell event could be potentially contaminated by the microseismic noise, both signals being characterized by an elliptical particle motion in the horizontal plane.

In order to quantify the potential influence of such swell-related microseismic noise on the teleseismic shear wave splitting measurement, it is important to quantify the signal-to-noise ratio SNR1 of the SKS phase amplitude on the radial component related to the pre-event seismic noise amplitude. Such ratio will be indicative of the potential influence of the swell-induced ground polarization into the SKS-induced ground polarization. We analysed the seismic noise using the data preceding the *P*-wave arrival on the radial component, and we focused our analysis on the 26 events that provide good quality splitting measurements. We performed our analysis on about 10 min of data before the *P* wave, except for three events at PTCN and RAR where only 300 s were available for such noise measurement. On the raw signals, the measured SKS SNR1 varies from 0.9 to 18 with a mean of 5. The very low value of 0.9 corresponds to a particular event (2000 January 28) recorded at PTCN and characterized by a high frequency noise content. That event has been kept since the SNR ratio increased to 3 on the filtered data and provided a good splitting measurement. The SKS SNR measurements obtained on data filtered between 0.01 and 0.1 Hz provide SNR ranging between 3 and 128 with a mean of 26. Such high SNR clearly show that for all the 26 good non-null splitting measurements, the SKS signal clearly dominates the background noise in the same period range. This first argument suggests a very limited influence of the noise on the SKS splitting parameters. We also computed SNR2: the ratio of the radial signal amplitude (in the frequency band we usually perform our splitting measurements) to the radial SF noise. SNR2 ranges between 13 and 468 with a mean of 93. We found no correlation between the variation of SNR2 and the apparent splitting parameters variations suggesting very low influence of the swell related seismic noise on the measurements of anisotropy parameters.

The second critical parameter to be evaluated in this analysis of the swell/SKS signal interaction is the polarization direction of the pre-event, swell-related, microseismic noise compared to the teleseismic shear wave splitting measurements. Correlation of the azimuth of the fast split shear wave with the swell-induced ground motion polarization direction may imply that swell-related noise may be mapped as upper-mantle anisotropy. To evaluate the swell-related microseismic noise polarization direction, we use the principal component analysis described by Barruol *et al.* (2006) to characterize the 3-D elliptical ground motion. The azimuth of the swell-related microseismic noise is determined by the direction of the eigenvector corresponding to the maximum eigenvalue of the covariance matrix. We compute the degree of linear polarization in the horizontal (*CpH*) and in the vertical plane (*CpZ*) for each pre-event noise data, bandpass filtered in the SF band, between 0.05 and 0.077 Hz, that is, 13–20 s of period. These coefficients theoretically range from 0 to 1 and characterize the degree of linearity of a plane wave, a *CpH* value of 1 corresponding to a purely linear motion in the horizontal plane, and a value of 0 indicates a circular particle motion in the horizontal plane. About half of the pre-event noise measurements performed on the seismograms that provided good non-nulls SKS splitting measurements have $CpH > 0.85$ and $CpZ > 0.87$. This means that the swell-related noise in the SF band is characterized by a quasi-linear particle motion essentially in the horizontal plane. The azimuths obtained for the swell-induced ground polarization show however absolutely no correlation with the SKS fast direction that trend on average along NW–SE to WNW–ESE azimuth. Our measurements of swell-related noise polarization azimuths show instead clear correlation with the swell directions such as 195–212°E at REA, 235°E at ANA and 332°E at TAK. These values are fully consistent with those observed by Barruol *et al.* (2006), who, showed the presence of two dominant swell directions in French Polynesia: swells generated during the austral winter in the South Pacific and propagating across French Polynesia with azimuths between 200°E and 230°E, and swells generated in the northern Pacific during the boreal winter and propagating through

the South Pacific along azimuths ranging 310°E–330°E. From the 26 good events we analysed, only one measurement of swell polarization (at RKT), shows a similar direction as the SKS fast direction, but the very high SKS SNR value of 76 obtained on the filtered signal demonstrates that, although the SKS and microseismic noise are polarized along similar directions, the SKS amplitude is much larger. The noise polarization would, therefore, have a very limited influence on the measurement of the fast SKS azimuth. Even if the fast split direction is not similar to the swell direction, the splitting measurement could be partially contaminated by the swell noise. That may be the case especially if the swell direction is parallel to the great circle. However, the high SNR of the good non-null splitting measurements show that the SKS signal clearly dominates the background noise.

In summary, we find that the swell-related microseismic noise in the SF frequency band is often responsible for a well polarized signal in the horizontal plane but its much lower amplitude compared with the SKS signal as well as the absence of correlation between the direction of fast split shear wave and the direction of swell-related microseismic noise polarization suggest that the swell has very limited influence on the shear wave splitting measurements.

3 RESULTS: SHEAR WAVE SPLITTING IN THE SOUTH PACIFIC

Analysis of individual splitting measurements yields resolvable delay times at all stations except at PPT and PPTL on Tahiti (the GEOSCOPE and LDG/CEA sensors are a few metres from each other) and at TAOE, a GEOSCOPE/CEA station recently installed on Nuku Hiva in the Marquesas. In this section, we first describe the results obtained by the single event analysis (examples shown in Fig. 3) with subsequent determination of weighted averages, following Silver and Chan (1991) weighting each individual non-null measurement by its σ_Φ and $\sigma_{\delta t}$ (Table 1). We then present the results obtained by the stacking technique (example presented in Fig. 4) that allows to compare our results with those previously published by Wolfe & Silver (1998). Table 1 lists, for both the weighted average method and the stacking procedure, the number of events used and the splitting parameters.

3.1 Single event analysis

The individual splitting parameters measured at each station can be found in Tables 2 and 3. Fig. 5 presents the map of the individual and stacking splitting measurements. We present in Fig. 6 the distribution of the null measurements for 12 seismic sites: all permanent seismic sites and some PLUME stations. The chosen PLUME stations are characteristic of the backazimuthal coverage observed at the PLUME portable stations. The null measurements are observed for a wide range of backazimuths and are not clustered around the fast/slow directions. This dispersion may be due to the influence of oceanic seismic noise. In this study, interpretation of mantle structure is, therefore, essentially based on good quality non-null measurements.

3.1.1 Marquesas (HIV and TAOE)

The origin of the Marquesas archipelago is still debated since it displays contradictory features. The progression of age of the volcanic edifices along the archipelago (Duncan & McDougall 1974) suggests the presence of a plume close to the Marquesas Fracture Zone, but the absence of recent volcanic activity in this area together with a general island alignment (N40°W) not parallel to the present Pacific Plate motion (N65°W) imply a more complex origin for these islands (e.g. Brousse *et al.* 1990). Station HIV is located at *ca.* 270 km north of the Marquesas Fracture Zone. The fast polarization direction is oriented N74 ± 18°E (Fig. 5), close to the fossil spreading direction (N75°E) and to the Marquesas Fracture Zone orientation, but distinct from the general N40°W trend of the volcanic island chain. This station unfortunately provided only one well-constrained measurement and thus we cannot exclude possible backazimuthal dependence of splitting parameters. The limited data available at TAOE (recording since December 2004) provides only one null measurement at TAOE for a backazimuth of N264°E.

3.1.2 Tuamotu (MAT, TPT, TAK, ANA, HAO and REA)

The Tuamotu archipelago is composed of numerous atolls located on a large oceanic plateau. This plateau trends roughly parallel to the Pacific Plate motion but its origin is probably much older than the other Polynesian volcanic alignments, perhaps related to hotspot activity occurring about 50 Ma ago on a young lithosphere close to the Farallon ridge (Ito *et al.* 1995). Our results at the Tuamotu stations show large variations of splitting parameters: Φ varies from N53°W to N106°W and δt ranges from 0.85 to 2.70 s (Table 2 and Fig. 5). At TPT, which is not running since 1996, a single constrained value was obtained by Russo & Okal (1998) and we did not find any other resolvable splitting with the single event analysis.

All stations except REA and TAK show an average fast polarization direction weighted by σ_Φ and $\sigma_{\delta t}$ (Table 1) close to the present Pacific APM direction [ranging between N65°W and N70°W depending on the stations location (Gripp & Gordon 2002)]. Individual measurements display however a rather strong dispersion even within the good quality measurements (Table 2 and Fig. 5). This is particularly clear for good measurements obtained at ANA Φ = [N53°W, N75°W], HAO Φ = [N53°W, N96°W], REA Φ = [N64°W, N106°W] and for fair quality measurements at TAK Φ = [N41°W, N116°W]. This dispersion may result either from the presence of two or more horizontal layers of anisotropy and/or from lateral heterogeneities beneath these stations.

REA and TAK (located *ca.* 140 km south of the Marquesas Fracture Zone) show good quality fast polarization directions close to the orientation of this fracture zone: N74 ± 6°E and N64 ± 9°E, respectively. On the other hand, stations MAT and TPT that are closer to this ancient transform fault (*ca.* 70 and 115 km, respectively) show fast polarization azimuths subparallel to the APM direction (mean parameters in Table 1). However, only a single non-null measurement was obtained at both MAT and TPT. Therefore, we cannot conclude that mantle structure related to the Marquesas transform is not present below MAT and TPT.

A difference in both fast polarization orientation (25°) and delay time is observed at REA from independent and well-constrained SKS and SKKS measurements. A similar difference on fast polarization direction for SKS and SKKS is observed for the same event at ANA, but the incertitude on the splitting parameters is much larger. Variation in the splitting parameters obtained from SKS and SKKS phases from the same event has been already described in the literature (e.g. Barruol & Hoffmann 1999; Niu & Perez 2004) and could result from lowermost mantle anisotropy, since the paths of the two phases are different in D″ (e.g. Hall *et al.* 2004). At REA, both SKKS and SKS piercing points at the core–mantle boundary towards the receiver-side are located east of the Tonga/Fiji subduction zone. For the same event at ANA, the SKKS piercing point is located on the

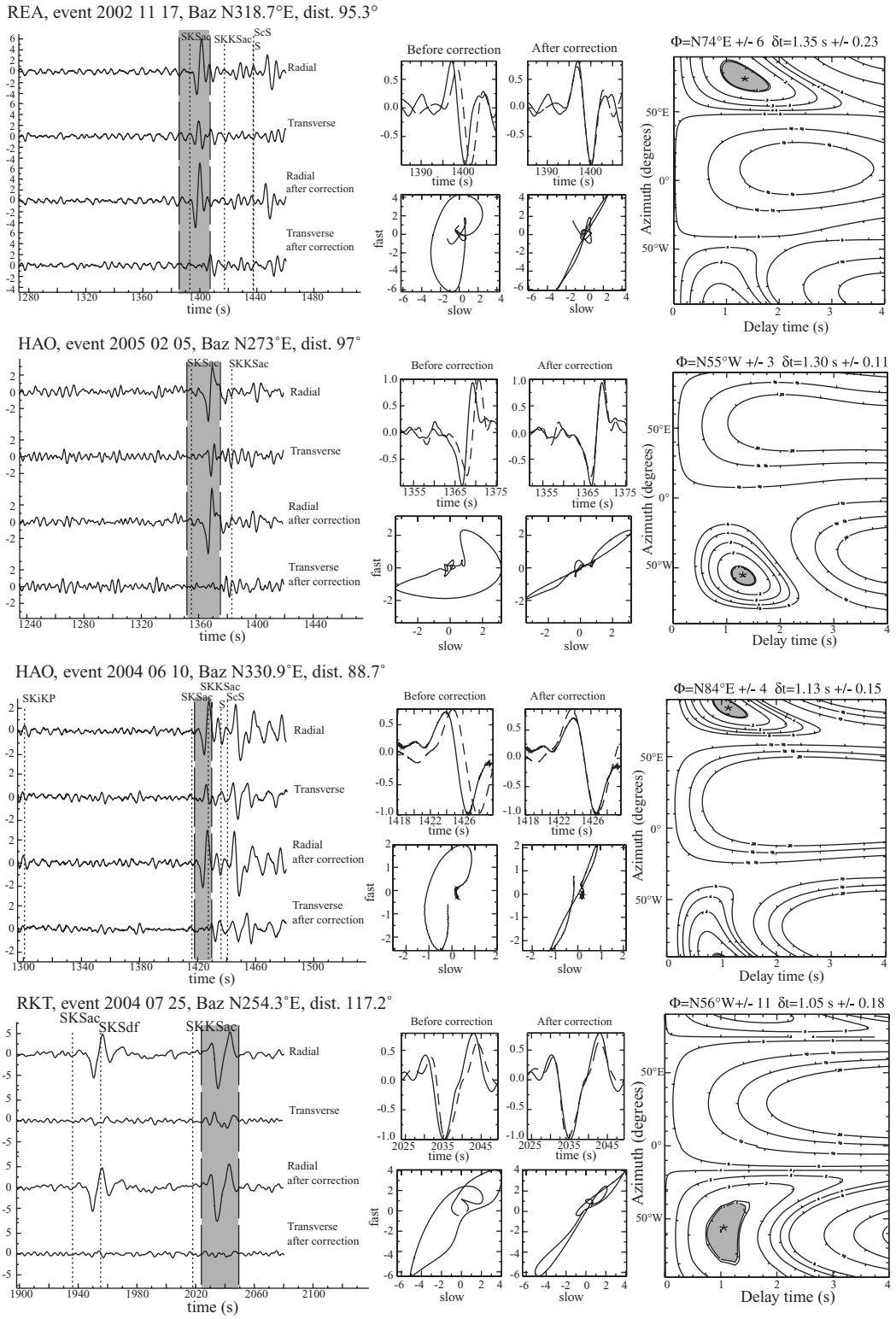

Figure 3. Examples of individual splitting measurements obtained from the single event analysis at stations REA, HAO and RKT. For each measurement we show on the left the radial and transverse components before and after the anisotropy correction. The shaded rectangles represent the time windows used in the analysis. Note the removal of energy on the transverse component after correction. The four diagrams on the middle panel plot the fast and slow split shear waves (continuous and dashed line, respectively) raw and corrected for the best-calculated delay time. Particle motions in the horizontal plane are shown below, also uncorrected and corrected for the anisotropy; the elliptical particle motion becomes rectilinear when the anisotropy is corrected. The right panel represents the contour plot of energy on the transverse component as a function of the delay time δt (seconds) and the polarization angle Φ (degrees) of the fast split shear wave. The double contour represents the 95 per cent confidence interval. The backazimuthal dependence of the splitting parameters, used to test models of two anisotropic layers, is illustrated by the two measurements obtained at HAO. The event arriving from the West provides a fast azimuth oriented N55°W whereas the event arriving from NW provides a fast azimuth oriented N84°E.

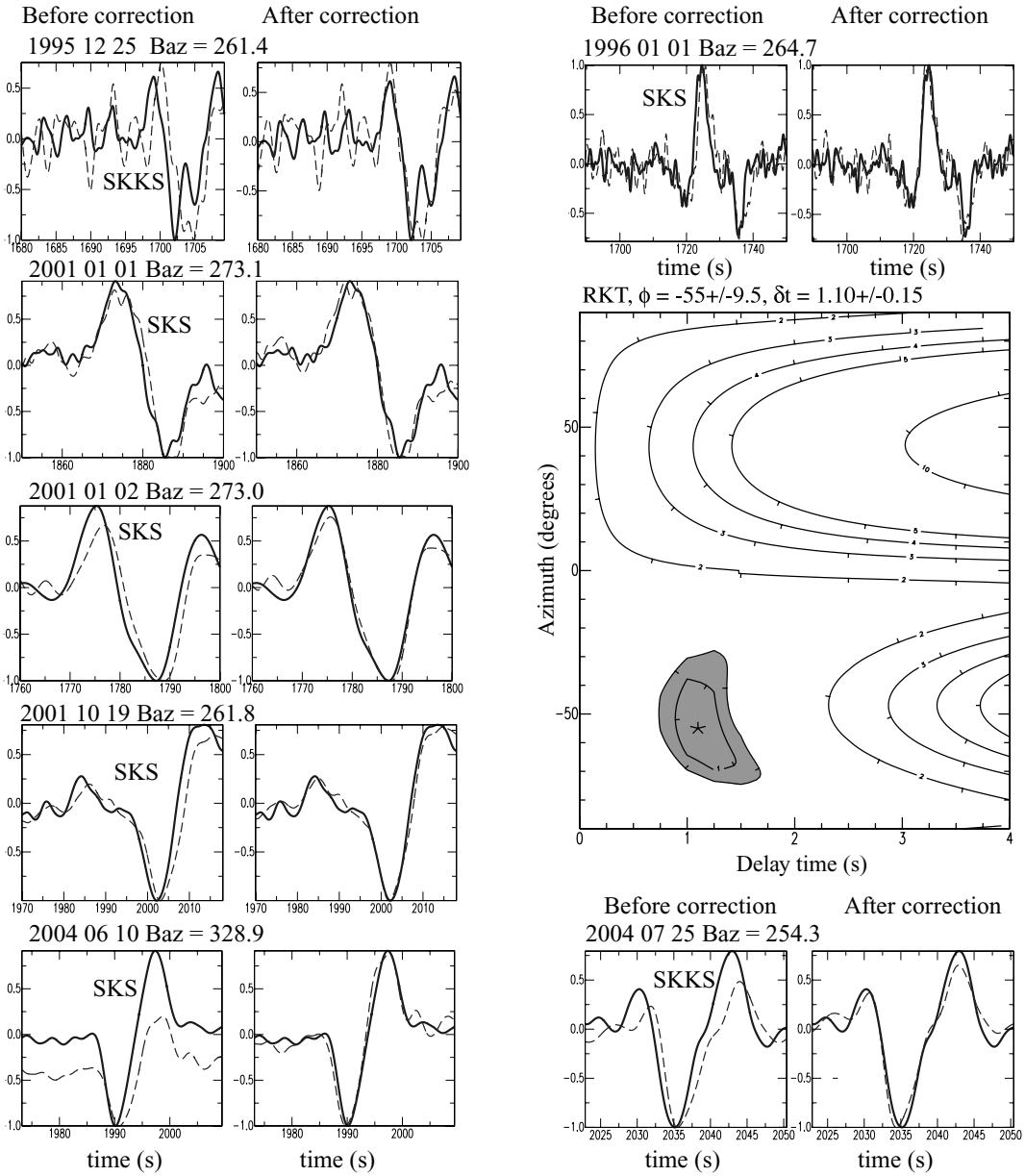

Figure 4. Example of 'stacked' splitting measurements using the Wolfe & Silver (1998) method at the LDG/CEA RKT stations in the Gambier Islands. For each of the seven events taken into account in this measurement are plotted the fast (thick line) and slow (thin line) split shear wave before and after anisotropy correction. On the contour plot, the dark region corresponds to the 95 per cent confidence region.

Tonga/Fiji subduction zone, whereas the SKS piercing point is east of the subduction zone.

3.1.3 Gambier-Pitcairn (PTCN and RKT)

Located at the southeasternmost tip of the Tuamotu archipelago, the Gambier Islands have an origin different from that of the Tuamotu atolls. This young volcanic alignment is interpreted as resulting from the activity of the Pitcairn hotspot (e.g. Dupuy *et al.* 1993; Clouard & Bonneville 2005). The average fast polarization direction varies from N54°W at RKT to N84°W at PTCN (Table 1), not far from the orientation of the hotspot-related volcanic alignment: N65°W. Similar average delay times are observed at RKT and at PTCN, about 1.2 s. We observe a dispersion of fast polarization direction at PTCN, where Φ varies from N47°W to N97°W and at RKT, where Φ ranges from N41°W to N74°W (Table 2 and Fig. 5). As discussed below, variation of splitting parameters obtained on good quality measurements may be due to the presence of several layers of anisotropy beneath the stations and/or to small-scale lateral variations in the mantle structure. For both stations we observe fast polarization directions similar to the local present-day APM direction, that is around N70°W. Only PTCN shows some orientation of the fast shear wave close to the E–W direction. A difference between fast polarizations determined from SKS and SKKS phases is also observed at RKT, but this difference is poorly constrained due to the high σ_Φ of the measurements.

3.1.4 Society (MA2, PPT and PPTL)

The Society archipelago is aligned along the trend of the present-day Pacific Plate motion and the island ages decrease linearly towards the Society hotspot (e.g. Duncan & McDougall 1976; Diraison *et al.*

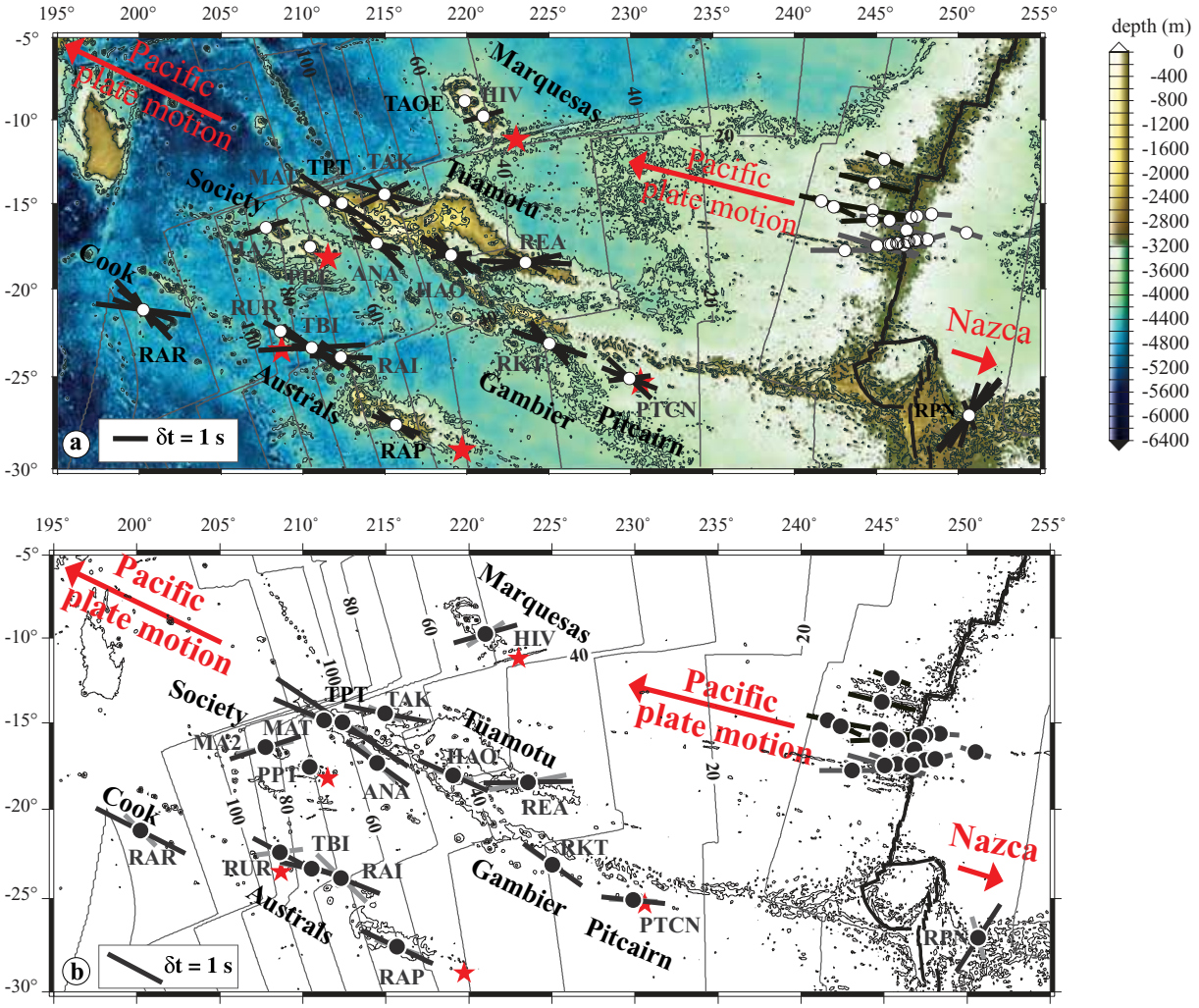

Figure 5. Map of the SKS splitting measurements measured at permanent and temporary stations in the South Pacific. Circles represent the seismic stations and stars the presumed hotspots locations. The azimuth of each bar represents the fast split direction and its length the delay time between the two split arrivals. (a) Map showing all the non-null individual measurements (presented Table 2). (b) Map showing the average splitting parameters obtained at each station from the multi-event stacking technique (grey bars) from Wolfe & Silver (1998) and in black from the Silver & Chan (1991) weighted mean calculation (Table 1). Together with the new results from the present paper are plotted the measurements obtained from two ocean bottom experiments close to the East Pacific Rise: the MELT (Wolfe & Solomon 1998) and GLIMPSE experiment (Harmon *et al.* 2004).

1991), presently located 70–130 km east of Tahiti (Talandier & Kuster 1976). Although 15 yr of data have been studied at stations PPT and PPTL on Tahiti Island, we failed to observe any detectable splitting ($\delta t \leq 0.2$ s). This apparent isotropy or weak anisotropy confirms the results from previous studies (e.g. Russo & Okal 1998; Wolfe & Silver 1998; Barruol & Hoffmann 1999). On Maupiti Island, the northwesternmost island of the Society archipelago, we obtained $\Phi = 72 \pm 5°$E, a direction close to the fossil spreading direction (N75°E) and to the orientation of the neighboring Marquesas Fracture Zone, although this station (MA2) is more than 100 km away from the fracture zone.

3.1.5 Cook-Austral (RAR, RUR, TBI, RAI and RAP)

The Austral archipelago displays a general alignment parallel to the Pacific Plate motion direction that could suggest a simple origin from the Macdonald hotspot (e.g. Duncan & McDougall 1976), but recent geochemical and geophysical data indicate a more complex history implying several short-lived hotspots (Bonneville *et al.* 2002; Clouard & Bonneville 2005). The weighted mean values of the fast polarization azimuth range from N62°W to N77°W. These values are close to the direction of the present Pacific APM. Scattering of fair quality measurements obtained on data from different backazimuths is observed at both RAR $\Phi = [$N30°W, N83°W$]$ and TBI $\Phi = [$N53°W, N97°W$]$. These variations may be due to the presence of several layers of anisotropy and/or of lateral heterogeneities. TBI, located 70 km north from the Austral Fracture Zone, provides good quality fast polarization directions in the range N83°E–87°E. The trend of the Austral Fracture Zone being *ca.* N70°E, these fast polarization directions could reflect the influence of the fracture zone on the mantle flow. RUR provides only one non-null measurement, which is compatible with the measurements obtained at TBI and RAP. At RAI, as in ANA, REA and RKT, we observe a large difference in splitting parameters deduced from SKS and SKKS phases from the same event, Φ being N88 $\pm$ 9°W and N53 $\pm$ 8°W, respectively. The difference of fast polarization orientation is well constrained and may be due to lower mantle anisotropy and/or a dipping axis of anisotropy. The SKKS piercing point of this event at the

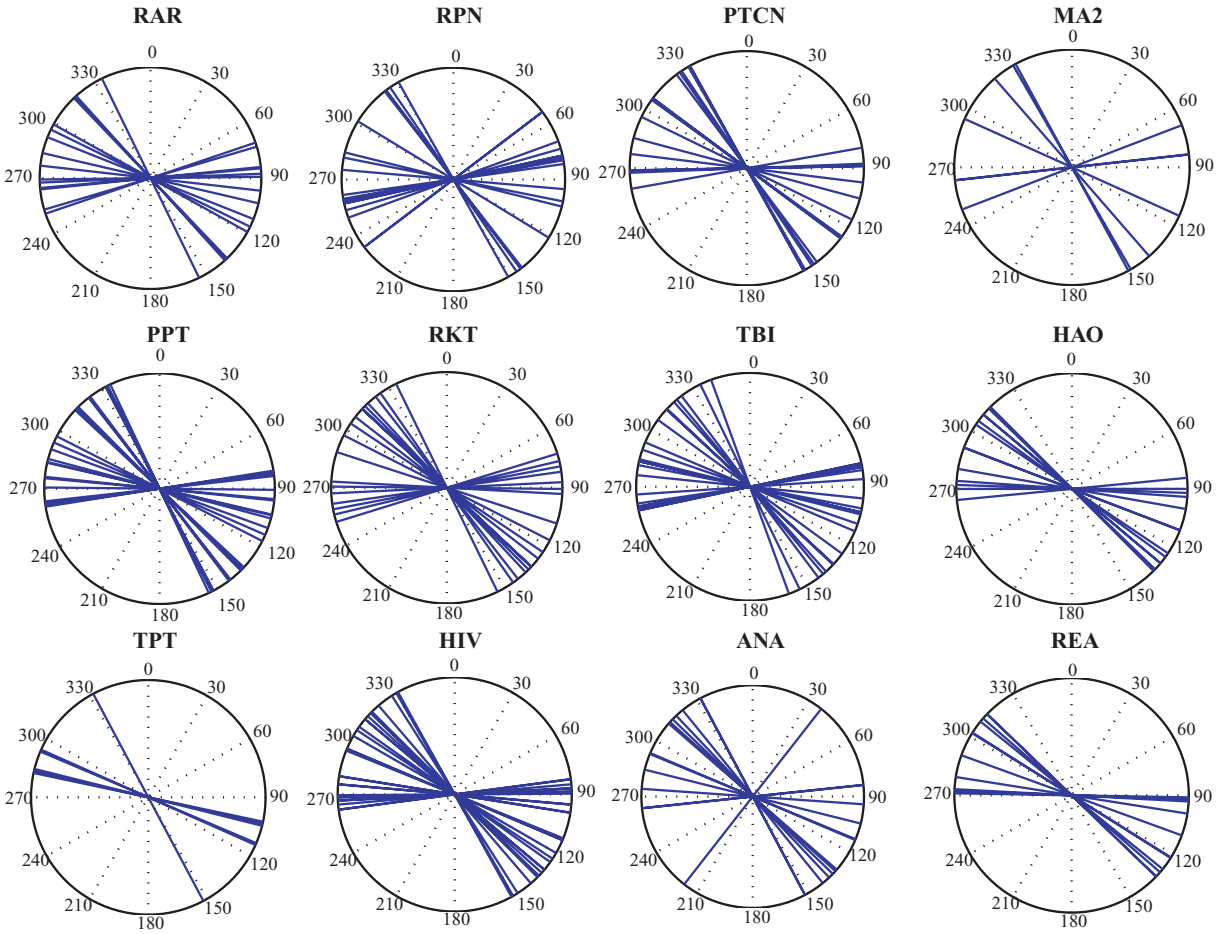

Figure 6. Distribution of null measurements at 12 seismic stations: all permanent seismic sites and some selected PLUME portable stations.

core–mantle boundary is, located in the vicinity of the Tonga/Fiji subduction zone whereas the SKS piercing point is east of the subduction zone.

3.1.6 Easter Island (RPN)

RPN station on Rapa Nui or Easter Island is located on the Nazca Plate, at *ca.* 250 km east of the East Pacific Rise. The measured fast polarization directions at RPN vary from N22°W to N47°E. We observe a clockwise rotation of the apparent fast polarization direction with an increase of backazimuth. This dependence of the apparent polarization direction to backazimuth and the high dispersion of measurements are characteristic of the presence of several layers of anisotropy with horizontal fast axis below the station.

3.2 Mean splitting parameters in French Polynesia

From the individual splitting measurements presented above, we calculated the mean splitting parameters at each station by weighting the results by their uncertainties. We then used these mean splitting parameters to calculate the median values of anisotropy parameters in French Polynesia, which produces an estimate of central tendency of splitting parameters at the scale of the network. We exclude RAR and RPN from this calculation, since RPN is not located on the Pacific Plate and the lithosphere beneath RAR is probably characterized by a fossil spreading direction close to NS (e.g. Viso *et al.* 2005). Computing median values assumes inherently that there is only one layer of anisotropy beneath French Polynesia. This helps to characterize the first-order structuration of the shallow mantle beneath the South Pacific.

The observed delay times throughout the Polynesian area range from 1.05 to 2.70 s (Table 1) with a median value of 1.33 s. The median value for the azimuth of the fast split shear wave is N68°W. This value accounts for the lower weight of the two extreme values observed at HIV (Φ = N74°E) and at MA2 (Φ = N72°E). Interestingly, this median value is parallel (<1° difference) to the mean value of the present-day Pacific APM in French Polynesia (N67°W) (Gripp & Gordon 2002). This correlation suggests that the first order signal carried out by the orientation of the SKS fast polarization directions is the deformation induced by the motion of the Pacific Plate relative to the asthenosphere, which is well characterized by the APM in the hotspot frame. This central tendency of fast polarization directions is consistent with Rayleigh wave azimuthal anisotropy observations that also shows an agreement of the fast Rayleigh propagation directions with the plate motion at asthenospheric levels, that is, between 100 and 300 km depth (e.g. Nishimura & Forsyth 1989; Smith *et al.* 2004; Maggi *et al.* 2006a) and with numerical modelling of the development of anisotropy by asthenospheric deformation by drag from a moving plate (Tommasi 1998). Even though these observations suggest that the dominant signal carried out by the orientation of the SKS fast polarization directions is, at first order, the deformation induced by the motion of the Pacific Plate relative to the asthenosphere, we observe variations of the splitting parameters with backazimuth and we show in

the following of this paper that these variations are consistent with two-layer models of anisotropy which could explained up to 44 per cent of the observed variations.

3.3 Multiple events investigation

As explained above, the 'stacking' technique takes into account several events to find the best Φ and δt parameters compatible with the individual measurements. Stations displaying backazimuthal dependence of the splitting parameters have, however, to be considered with care since this method may then provide unrealistic averages of the splitting parameters. This technique has been shown however to be useful in oceanic environments (Wolfe & Silver 1998) since (i) the microseismic noise is generally rather high and may hide the small transverse component of the split phase, (ii) some stations do not provide any resolved splitting with the single event method (such as PPT) and (iii) other stations provide a very limited number of well constrained measurements (such as HIV, MA2, MAT, TPT and RUR). The results obtained from this stacking technique are summarized in Table 1. They show similar results to the Silver & Chan (1991) average values, except at RPN, RAI and RUR for which large differences ranging from 22° to 49° are found.

The multiple events procedure yielded results at RAR and RPN stations (Table 1) similar to previous SKS splitting measurements by Wolfe & Silver (1998) and to the fast polarization azimuth deduced from *P*-wave polarization deviations at RPN (Schulte-Pelkum *et al.* 2001). Our measurements at TBI, RKT and TPT are consistent with those of Russo & Okal (1998). However, at PTCN, our fast direction is hardly compatible (difference of 49°) with their observation. Such difference could be due to the fact that we use more events than these authors, and particularly three recent events that provide good quality measurements with Φ trending EW, but also that we did not take into account any direct *S* phases in the stacking procedure. The apparent isotropy we observe at PPT was already described by previous studies using both the stacking (Russo & Okal 1998; Wolfe & Silver 1998) or the single event methods (Barruol & Hoffmann 1999).

In the following discussion, we will only consider the results from single event analysis as we have seen that the presence of multiple anisotropic layers is possible beneath French Polynesia.

4 DISCUSSION

4.1 Possible causes of seismic anisotropy in oceanic basins

The simplest model to explain the development of a pervasive fabric (or olivine crystal preferred orientations) invokes shearing of the sublithospheric mantle in response to a velocity gradient between the plate (rigid lithosphere) and the asthenosphere. Progressive cooling of the plate freezes the olivine crystal preferred orientation (CPO) within the plate and results in deepening of the shear zone. This process aligns the olivine [100] axes, and, therefore, the polarization of the fast split shear waves parallel to the absolute plate motion direction. In this model, the observed delay times should thus increase with lithospheric age (Tommasi 1998). This simple model is probably not fully appropriate for the Pacific, which suffered an important plate reorganization at the end of Cretaceous (Mammerickx & Sharman 1988; Mayes *et al.* 1990) and changes in the spreading direction during the Oligocene (e.g. Mayes *et al.* 1990). Variations in the APM direction are expected to create different layers of anisotropy, the most superficial one corresponding to the older plate motion and the deepest corresponding to the present-day asthenospheric flow (Tommasi 1998; Rümpker *et al.* 1999). The boundary between the two anisotropic layers should lie within the lithosphere, its depth depending on the age of the lithosphere at the time of the change in plate motion. The sublithospheric mantle may be in motion which means that the fast polarization direction is parallel to the vector difference of the lithosphere and the sublithospheric mantle motion (Silver *et al.* 2001).

Transform faults may locally perturb the asthenospheric flow since they represent a vertical boundary between lithospheres of different ages and, therefore, of different thicknesses that may locally channel the sublithospheric flow (Sleep 2002). Hotspot activity and the related mantle upwelling should also modify the sublithospheric flow. Indeed, the rising mantle material may spread beneath the moving lithosphere. The interaction between the upwelling mantle and the horizontal displacement of the lithosphere is proposed to induce a parabolic asthenospheric flow (Ribe & Christensen 1994), which should be visible in the shear wave splitting measurements if the station coverage is dense enough (Walker *et al.* 2005b). The geometrical characteristics of this parabolic flow depend on the velocity of the plate motion and also on the strength of the plume-induced mantle flux (Ribe & Christensen 1994; Ribe & Christensen 1999). The presence of penetrative partial melt could also produce additional anisotropy in the sublithospheric mantle due to an alignment of melt-rich domains or result in a change in olivine deformation patterns (Holtzman *et al.* 2003; Fontaine *et al.* 2005). In addition, it has been proposed that mantle plumes may locally destroy or at least modify the lithospheric anisotropy by reheating and thinning of the lithosphere (Sleep 1994; Thoraval *et al.* 2006). Melt-rock interaction in the lithospheric mantle, on the other hand, should preserve seismic anisotropy, except in local melt accumulation horizons (Tommasi *et al.* 2004).

4.2 Comparison with previous seismic measurements of anisotropy in the Pacific

Seismic refraction experiments performed few decades ago in the northern Pacific yielded *Pn* azimuthal anisotropy, with fast *P*-wave velocities parallel to the transform faults and normal to the magnetic lineation, that is, parallel to the palaeospreading direction, suggesting alignment of the olivine [100] axes at high angle from the ridge trend by the asthenospheric flow (Hess 1964). These fast *Pn* directions are roughly EW north of Hawaii (Hess 1964; Francis 1969; Raitt *et al.* 1969) and close to N150°E in the northwestern part of the Pacific (Shimamura & Asada 1983). Since seismic refraction uses *Pn* waves travelling within the uppermost part of the lithospheric mantle, this technique is unable to provide information on the deeper structure of the lithosphere and on the asthenospheric flow that could correspond to the present-day plate motion.

Splitting of teleseismic shear waves has been measured at several places in the Pacific basin. In Hawaii, on a 90 Ma old lithosphere, the SKS splitting observations obtained at the GEOSCOPE station KIP (Wolfe & Silver 1998; Barruol & Hoffmann 1999; Walker *et al.* 2001) provide results compatible with two layers of anisotropy, a lower layer with a fast azimuth parallel to the present-day Pacific APM direction and an upper layer with a fast azimuth close to the palaeospreading direction, therefore, compatible with the fast *Pn* directions. Experiments deployed in the vicinity of the East Pacific Rise show primarily fast shear wave polarizations parallel to the present spreading direction (Wolfe & Solomon 1998; Harmon *et al.* 2004). By using splitting of *PS* phases from deep Tonga events recorded at North American stations, Su & Park (1994) measured

a fast anisotropy orientation close to the APM direction. In French Polynesia, Russo & Okal (1998) perform splitting measurements at four permanent IRIS, GEOSCOPE and CEA/LDG stations and yield NW–SE fast split shear wave directions compatible with an asthenospheric origin, but with rather strong variations from station to station they attribute to short-scale variations in the upper-mantle penetrative structure related to the presence of the hotspot in this area.

Rayleigh wave azimuthal anisotropy provides a way to globally map the Pacific upper mantle with a good vertical sensitivity but with a lateral resolution of several hundreds of kilometres. They are, therefore, complementary to SKS waves that have lateral resolutions of few tens of kilometres but no vertical resolution. The first surface wave anisotropic models derived from few hundred seismic path crossing the Pacific (e.g. Montagner 1985; Nishimura & Forsyth 1988; Nishimura & Forsyth 1989) already showed an azimuthal anisotropy correlated to the palaeospreading direction at short periods and a better correlation to the present-day plate motion at longer periods, that is, at greater depth. More recent inversions using several ten thousands of seismic ray paths provide a better lateral resolution in the Pacific ocean and confirm the presence of two layers of anisotropy (Trampert & Woodhouse 2003; Smith *et al.* 2004), but they also give evidence of lateral variations of velocity and anisotropy that could be related to channeling of mantle flow (Montagner 2002) or to hotspot-related mantle upwelling (Maggi *et al.* 2006a).

4.3 Fossil anisotropy

As the oceanic plate cools, sublithospheric anisotropy is expected to be progressively frozen at the bottom of the lithosphere and the shear zone accommodating the velocity gradient between the plate and the deeper asthenosphere is progressively displaced towards larger depths. If the plate motion direction and velocity are constant through time, anisotropy should be homogeneous over the entire plate and sublithospheric mantle (Tommasi 1998).

For the Pacific Plate, the orientation of the present-day APM is close to the present-day spreading direction and one can assume that the same geometrical relationship existed before the plate reorganization that occurred roughly at magnetic anomaly 7 (25–26 Ma), (e.g. Mayes *et al.* 1990). In this simple model, the lithospheric strain for old (>25 Ma) French Polynesia seafloor, and therefore, the olivine [100] axes, should align close to the palaeoexpansion direction, underlined by the fracture zones.

In the South Pacific, the Marquesas and the Austral Fracture Zones are oriented N75°E and underline the Pacific-Farallon spreading direction between 100 and 25 Ma. At the proximity of the fracture zones (TBI, TAK, MA2 and HIV) some fast directions (ranging between N64°E and N83°E) are observed to be close to the orientation of this frozen tectonic structure, consistent with the presence of a fossil anisotropy in the uppermost mantle. At larger distance from the fracture zones, as for instance at HAO, REA and PTCN, we also observe some fast polarization directions close to the palaeospreading direction (between N74°E and N85°E), suggesting that a ENE fossil anisotropy is pervasively present in the lithosphere beneath French Polynesia.

4.4 Testing two-layer models: forward approach

The presence of several layers of anisotropy with horizontal fast directions beneath a given station is expected to produce an azimuthal variation of the splitting parameters Φ and δt that are obtained under the assumption of a single anisotropic layer (Silver & Savage 1994; Rümpker *et al.* 1999). Such a structure may, therefore, explain the apparent scattering observed at the South Pacific seismic stations. In the Pacific Ocean, two-layer models have been already proposed to explain the apparent variation of splitting parameters observed at station KIP on Oahu Island (Wolfe & Silver 1998; Barruol & Hoffmann 1999; Walker *et al.* 2001). As pointed out by previous studies (e.g. Hartog & Schwartz 2001), it is theoretically not possible to determine a unique model from observations of apparent splitting parameters without independent constraints. However, use of *a priori* geophysical constraints, as for instance the plate motion direction, allows determining families of plausible geodynamic models.

In order to compensate for the small number of events for testing the presence of two anisotropic layers beneath French Polynesia, we group the splitting observations over the entire network. This appears appropriate since a two-layer modelling requires better backazimuth coverage than we have at each individual station, and also since we want to decrease the influence of the seismic noise that is inherent in all the individual measurements. Indeed, we observe homogeneous fast split shear wave directions across the network for each range of event backazimuths (Fig. 7). We use a forward approach to evaluate the presence of two layers of anisotropy beneath French Polynesia considering measurements obtained for five events which provide evidence of splitting at several stations together (RAI, ANA, MA2, TAK, REA, PTCN, HAO, RAP, TBI, RUR and RKT). When two different measurements were available for the same event and at the same station for both SKS and SKKS phases, we decided to use the best-constrained measurement (lowest incertitude of both Φ and δt). We do not include in this approach results from RPN (on the Nazca Plate) and RAR [much older lithosphere with fossil spreading direction presumed to be close to NS (Viso *et al.* 2005)]. The present Pacific APM directions at the various seismic stations in French Polynesia range from N65°W and N72°W (e.g. Gripp & Gordon 2002), and the fossil spreading direction using magnetic isochrons is N75°E (e.g. Müller *et al.* 1997). We perform a grid search over the four parameters (Φ and δt for both the upper and lower layers) to determine the optimum model that may explain the observed backazimuthal variations of the splitting parameters. Following the scheme described by Silver & Savage (1994) and for a dominant signal frequency of 0.1 Hz, we compute the apparent splitting backazimuthal variation for each two-layer model, by varying in each layer the fast directions in steps of 2° (from 0°E to 180°E) and the delay time by steps of 0.2 s (from 0 to 2.6 s, which is our maximum observed value of delay time), providing a total of 1 353 690 models. To determine the 'best-fitting' model we have computed an appropriate misfit function for the two sets of parameters, $\sum(\Phi_{\text{observed}} - \Phi_{\text{calculated}})^2/\sigma^2{}_{\Phi} + \sum(\delta t_{\text{observed}} - \delta t_{\text{calculated}})^2/\sigma^2{}_{\delta t}$. The ratio of that function with respect to the one for the best-fitting model (Φ_{opt}, δt_{opt}) follows an F distribution, from which we determine the range of parameters that are within the 95 per cent confidence region, and thus acceptable. For each model, we also calculated the coefficient of determination R^2. As mentioned by Walker *et al.* (2004) the goal of R^2 is to estimate the degree to which two-layer models fit the splitting observations better than a single-layer model with horizontal fast axis.

$$R^2 = 1 - SSd/SSo, \tag{1}$$

where *SSd* is a sum of squares of the two-layer model misfit and *SSo* a sum of squares of the single-layer model (with horizontal

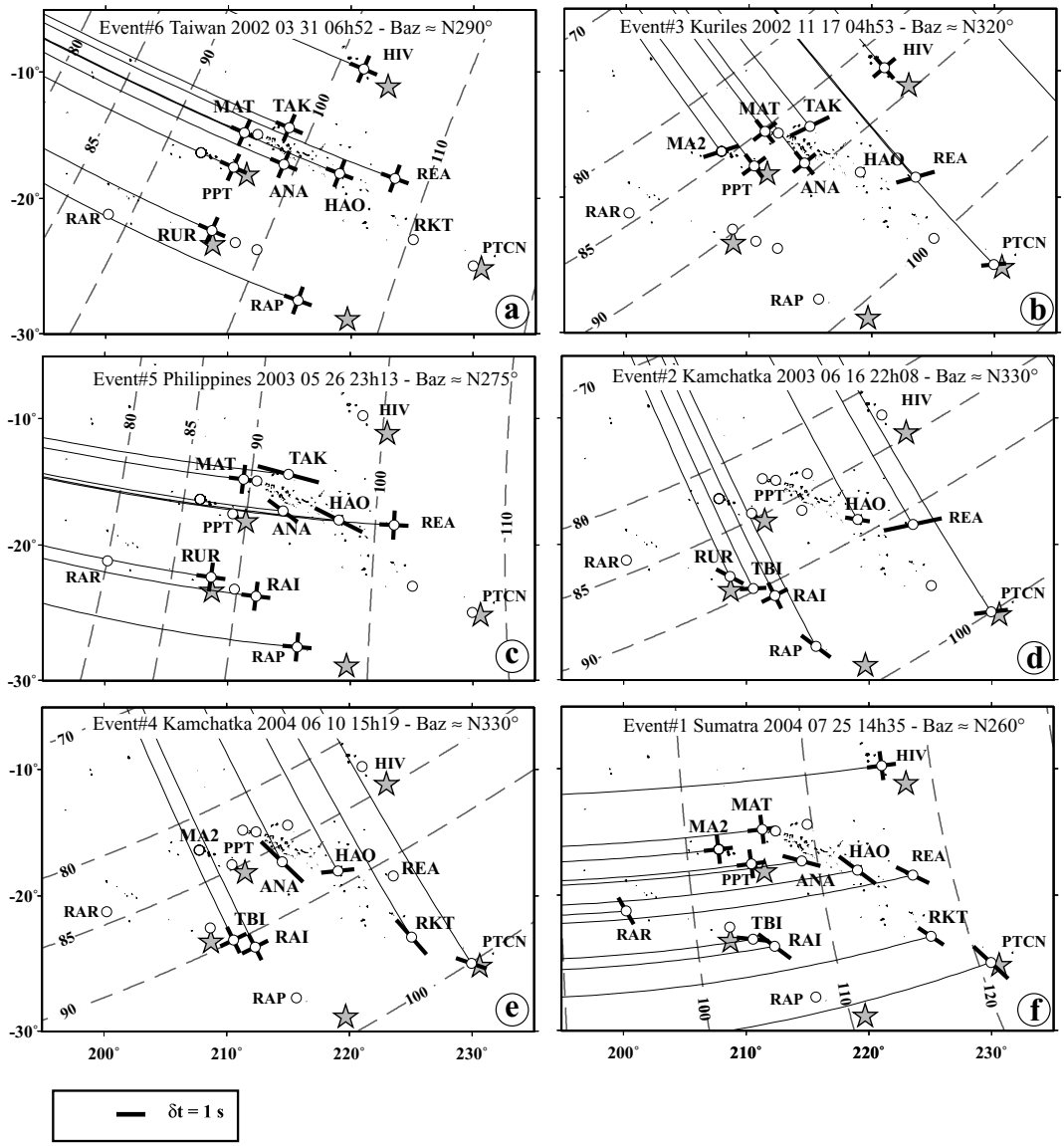

Figure 7. Maps of individual splitting measurements obtained at the PLUME and permanent stations for 6 particular events, sorted chronologically from (a) to (f). Circles represent the seismic stations and stars the presumed hotspots locations. The azimuth of the measured fast split direction is marked by the black line, and its length is proportional to the delay time. The maps also show the epicentral distances from the respective events. For some events, the minimum 85° epicentral distance is located in the middle of the network, explaining the absence of measurements at some stations located too close to the event. The Taiwan event (a) (backazimuth N293°E) provides high quality signals with consistently absent signal energy on the transverse component across the network (null measurements). The corresponding waveforms were already published in Barruol *et al.* (2002). This figure shows that the fast split directions are dependent on the event backazimuth, with fast directions trending ENE–WSW for backazimuths of N320°E (b) and NW–SE for backazimuths of N260°E (f).

axis).

$$SSd = \sum_1^N \left[\left(\frac{(\Phi_{\text{observed}} - \Phi_{2\text{ layer}})}{\sigma_\Phi} \right)^2 + \left(\frac{(\delta t_{\text{observed}} - \delta t_{2\text{ layer}})}{\sigma_{\delta t}} \right)^2 \right] \tag{2}$$

and

$$SSo = \sum_1^N \left[\left(\frac{(\Phi_{\text{observed}} - \Phi_{1\text{ layer}})}{\sigma_\Phi} \right)^2 + \left(\frac{(\delta t_{\text{observed}} - \delta t_{1\text{ layer}})}{\sigma_{\delta t}} \right)^2 \right] \tag{3}$$

σ_Φ and $\sigma_{\delta t}$ are the standard deviations of observed splitting parameters and N is the number of splitting measurements (i.e. 28 in our case). R^2 is the fraction of the total sum of squares that is explained. Theoretically and without the presence of seismic noise, this value ranges from 0 (no improvement by the two-layer model) to 1 (perfect fit). However, this number can be negative if the misfit of the single-layer model is lower than the misfit of the two-layer model. The determination coefficient can be biased by the number of independent variables. We therefore, compute a better coefficient, the adjusted R^2:

$$R^2_{\text{adjusted}} = 1 - (N_d - 1)(1 - R^2)/(N_d - k - 1), \tag{4}$$

where N_d is the number of observations (i.e. 2^*N) and k is the number of model parameters. This value is an index and can vary from $-\infty$ to 1. As is done by Walker *et al.* (2005a) we consider as statistically

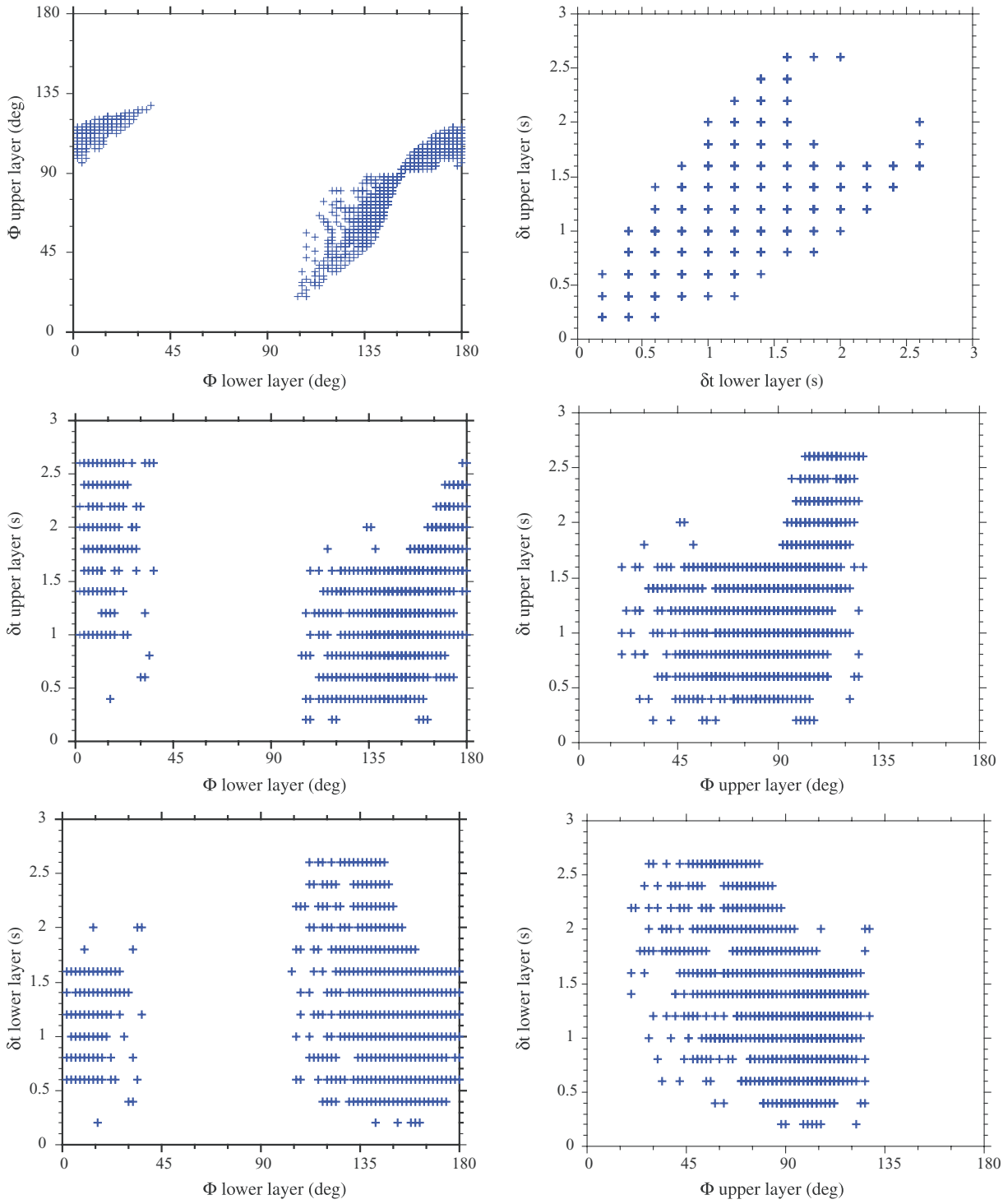

Figure 8. Distribution of the four splitting parameters for the two-layer models included in the 95 per cent confidence region from the multi-station two-layer modeling approach. The models represented as crosses are projected onto six pairs of splitting parameters axes. The model parameters are the fast polarization direction and delay time in the upper and lower layers. Each plot shows the projection of the 4-D parameter space onto a 2-D plane.

significant models which have $R^2_{\text{adjusted}} > 0.25$ (i.e. explaining more than 25 per cent of the variation).

Using the non-null measurements obtained for these five events from all stations except RPN and RAR, we obtained about 1156 models in the 95 per cent confidence region from more than 1 300 000 models. We only used non-null measurements in the two-layer modelling because the wide range of observed null backazimuths (Fig. 6) suggests a swell-related noise influence. We present in Fig. 8 the range of variations of the four splitting parameters for the two-layer models included in the 95 per cent confidence region. Values of the fast polarization direction for the upper layer lie in the range N20°E–N128°E, and for the lower layer in the range N104°E–N216°E. This indicates that the fast polarization directions are not well constrained neither in the upper nor the lower layer. The delay

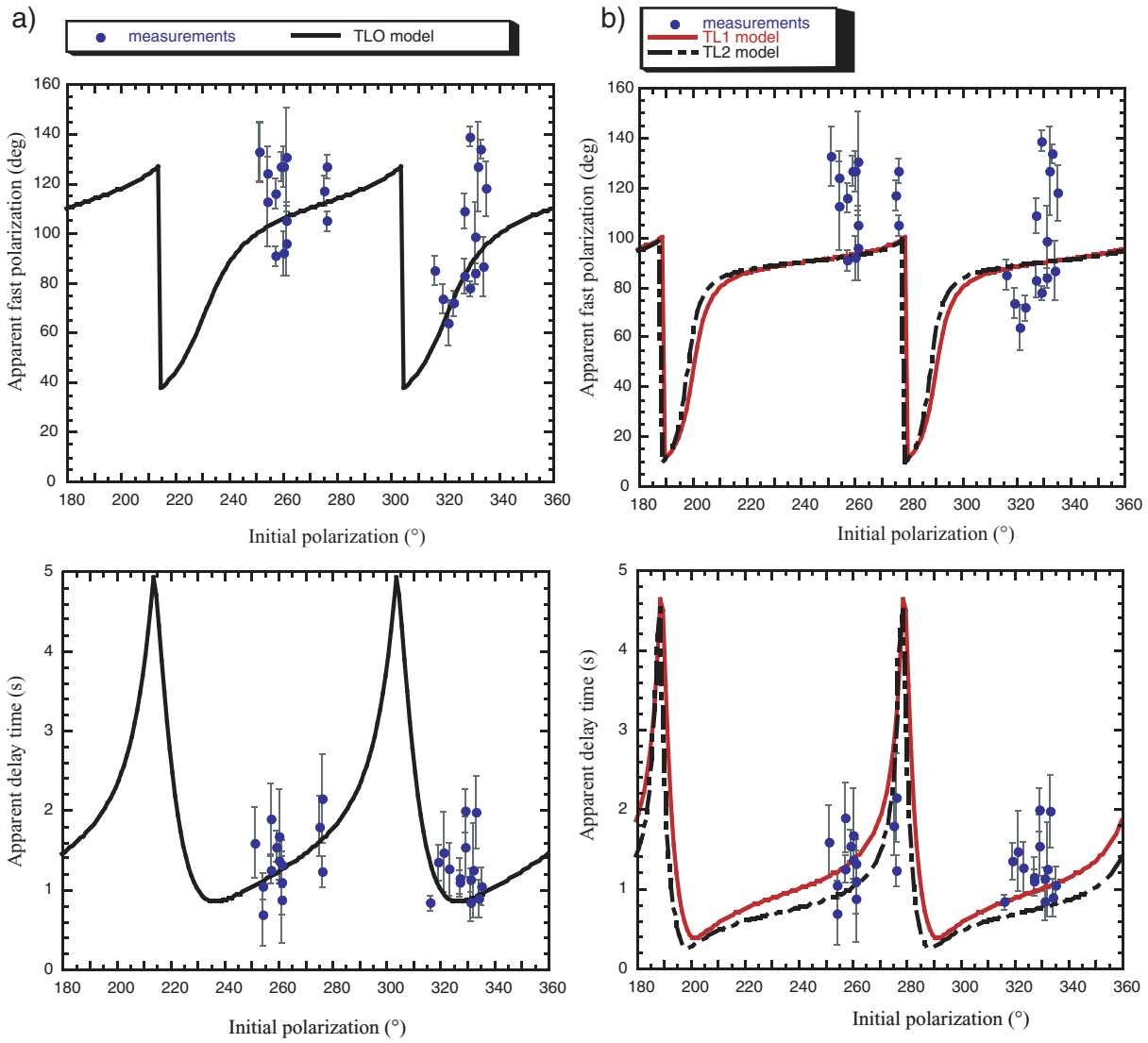

Figure 9. Fast polarization direction and delay time plotted as a function of incoming polarization direction. The measurements are from five events and several stations: RAI, ANA, MA2, TAK, REA, PTCN, HAO, RAP, TBI, RUR and RKT. (a) The computed splitting parameters for the best two-layer model TLO is shown for comparison with the measurements. (b) Measured splitting parameters are compared: (i) to a two-layer structure with Φ_{lower} close to the present-day Pacific APM direction and a contribution of fossil anisotropy in the upper layer (TL1) and (ii) to a two-layer structure with a contribution of small scale convection (TL2). See text for discussion.

time values for both layers lie in the range 0.2–2.6 s. Thus, the delay times are also not constrained. From the 1156 models, the optimum model (TLO) is characterized by $\Phi_{\text{lower}} = 136°\text{E}$, $\delta t_{\text{lower}} = 2.2$ s, $\Phi_{\text{upper}} = 54°\text{E}$, $\delta t_{\text{upper}} = 1.4$ s, $R^2 = 0.48$ and $R^2_{\text{adjusted}} = 0.44$. These values are displayed in Fig. 9(a) together with the individual splitting measurements. As illustrated in Fig. 9(a), we observe strong variations in the apparent fast polarization direction with event backazimuth rather than the gradual variation of splitting parameters that would be expected from dipping axis anisotropy, suggesting that such a dipping axis of anisotropy, if present, does not play a dominant role in the observations. Since a unique solution cannot be determined from the splitting measurements alone, we will use in the next subsections additional *a priori* informations and discuss the quality of fit and plausibility of acceptable classes of models. These models will compare observations to predicted values in the case of (i) fossil and present-day anisotropy contributions, (ii) small-scale convection and (iii) change of APM direction.

4.4.1 Fossil and present-day anisotropy contributions

Two-layer models proposed at KIP by large-scale surface wave tomographic models show that the azimuthal anisotropy within the upper lithosphere of the Pacific correlates well with the ridge spreading directions deduced from the magnetic anomalies whereas at asthenospheric depths, the azimuthal anisotropy is strongly correlated to the current mantle flow directions induced by the plate motion (Montagner & Tanimoto 1991; Smith *et al.* 2004; Maggi *et al.* 2006a). We select in the 1156 models belonging to the 95 per cent confidence region models for which the fast polarization direction in the lower layer is similar than the present-day Pacific APM direction. The best model (TL1 model) is characterized by $\Phi_{\text{lower}} = 114°\text{E}$, $\delta t_{\text{lower}} = 0.8$ s, $\Phi_{\text{upper}} = 66°\text{E}$, $\delta t_{\text{upper}} = 0.4$ s, $R^2 = 0.41$ and $R^2_{\text{adjusted}} = 0.36$. Fig. 9(b) shows that the fit is better for the apparent delay times than for the apparent polarization directions, although the dispersion of measured splitting parameters is high.

The best model for a fast anisotropic direction in the lower layer close to the APM have interestingly an upper layer with a fast direction close to the palaeospreading direction underlined by the fracture zones. This idea is in full agreement with the two-layer models observed for instance by surface wave tomography (Montagner & Tanimoto 1991; Smith *et al.* 2004; Maggi *et al.* 2006a).

4.4.2 Sublithospheric instabilities

In the case of a ridge axis with transform faults along the spreading center, numerical simulations from Morency *et al.* (2005) show that after 16 Ma, cold downgoing instabilities may develop at the base of the lithosphere. The orientation of the EPR ridge is N15°E. If we assume that these results obtained for plate velocities of 2–4 cm yr^{-1} are still correct at higher velocities, then the direction of the horizontal simple shear in the asthenosphere is mainly perpendicular to the ridge: N105°E in the lower layer. Due to the development of convection rolls, there is certain variability in the horizontal simple shear direction at the base of the lithosphere, but the shear direction is still mostly normal to the ridge axis. Additionally, the 3-D numerical simulations of Morency *et al.* (2005) suggest an upper layer with a direction between 10 and 20°E from the orientation of the ridge axis for lithospheric ages between 36 and 72 Ma. In the case of the EPR ridge, the direction in the upper layer could be between N25°E and N35°E. Assuming that similar instabilities are triggered in the South Pacific with a plate motion faster than the one used in the simulations, the best two-layer model (TL2 model) is characterized by $\Phi_{\text{lower}} = 106°\text{E}$, $\delta t_{\text{lower}} = 1$ s, $\Phi_{\text{upper}} = 28°\text{E}$, $\delta t_{\text{upper}} = 0.4$ s, $R^2 = 0.40$ and $R^2_{\text{adjusted}} = 0.35$. The quality of the fit is slightly less good than provided by TL1 model. The apparent splitting parameters obtained from this model are illustrated in Fig. 9(b) together with the observations.

4.4.3 Change in the APM direction

The bend displayed by the Hawaii-Emperor chain is usually interpreted as a record of a change in the Pacific APM at *ca.* 43 Ma. A similar shift is suggested in French Polynesia at the scale of the Tarava Seamounts (Clouard *et al.* 2003), the western part of the chain trends N20°W and the eastern part N60°W. We investigated in the 95 per cent confidence region two-layer models with a fast axis direction close to the present-day APM direction (±5°) in the lower layer and Φ_{upper} in the range N10°W–N30°W. However, we found no model corresponding to these criteria. Thus, as previously suggested by Tommasi (1998) a two-layer model of anisotropy associated with a change in the APM direction from N20°W to N60°W at 43 Ma does not seem adequate to explain the observed variations in the splitting parameters.

In summary, we cannot find a unique two-layer model, but our results suggest as follows.

(1) A two-layer structure of anisotropy explains the apparent splitting parameters variations better than a single layer with horizontal fast axis,

(2) An upper mantle with two layers of anisotropy cannot explain the totality of the splitting observations.

4.5 Testing plume-related upwelling and parabolic flow patterns

Recent surface wave tomographic models of the Pacific upper mantle (Maggi *et al.* 2006b) evidenced cylindrical low velocity anomalies down to at least 400 km depth beneath the Society and Macdonald hotspots that may result from mantle upwellings. These findings are compatible with body wave tomographic models described by Montelli *et al.* (2004) that argue for a Society hotspot rooted in the lower mantle. These mantle upwellings may spread beneath the lithospheric lid generating a parabolic asthenospheric flow due to a combination of the hotspot radial flow and the shear induced by the overlying plate displacement (Sleep 1990; Kaminski & Ribe 2002). Predictions from a parabolic asthenospheric flow pattern were compared with splitting data near Hawaii (Walker *et al.* 2001), in the Eifel region (Walker *et al.* 2005b), in the Yellowstone region (Waite & Schutt 2005) and beneath the Seychelles (Hammond *et al.* 2005). Testing such flow pattern in French Polynesia is unfortunately strongly limited by the sparse station coverage that does not provide the necessary short-scale observations, particularly around the hotspots, necessary to constrain the four parameters characterizing the flow field, that is, the plume strength, the plume centre, the plate velocity and the direction of plate motion. In the case of a fast-moving plate such as the Pacific Plate, the parabolic flow is expected to be extremely elongated along the APM direction and only stations above the mantle upwelling may distinguish such a model from that of simple asthenospheric flow. Additional stations such as the broad-band OBS deployed on the head of the hotspot (Suetsugu *et al.* 2005) may help to test this model.

4.6 Signature of ancient transform faults

The Marquesas and Austral Fracture zones represent frozen transform faults that were active at the Pacific–Farallon spreading ridge. Lithospheric age variation across these features is of 10–16 and 5–10 Ma, respectively (e.g. Mayes *et al.* 1990). In both cases, the older and therefore, thicker lithosphere lies on the northern side of the fracture zone. Using a simple assumption that the oceanic lithospheric thickness e is related to the plate age t through a relation such as $e = 9.1t^{0.5}$, (e.g. Fowler 1990) with e in km, t in Ma and for a thermal diffusivity of $0.804.10^{-6}$ m^2 s^{-1}, the lithospheric step between the ridge and a 10 Ma old lithosphere should be about 29 km. After 70 Ma, this step should be reduced to *ca.* 5 km (lower lithospheric layer in Fig. 10). This value is obviously a maximum estimate since lateral cooling and secondary convection (e.g. Sleep 2002) will tend to smooth the thermal gradient leading to a constant lithosphere thickness at old ages (e.g. Dumoulin *et al.* 2001). Close to a fracture zone and in the case of a young lithosphere, the asthenospheric flow beneath the lithosphere may be affected by this local relief and the orientation of this flow should be deviated towards the fracture zone direction. This local reorientation of the flow will depend on the wavelength of the relief, and therefore, on the age step across the fracture zone and on the age of the plate. In the case of French Polynesia, the older plate is leading the younger plate and we could expect a lower component of along-fracture-zone flow than in the case of a younger plate leading an older plate. However, some stations may potentially record fracture-zone parallel shear behind the step. Stations TBI and RAI that lie on both sides of the Austral fracture zone display indeed fast split shear waves polarizations deviating from the APM trend towards the fracture zone orientation. In the Society and Tuamotu archipelagoes, stations MA2 and TAK, both on the southern side of the Marquesas Fracture Zone display Φ trending almost parallel to the fracture zone direction, like station HIV in the Marquesas, north of the Marquesas Fracture Zone. Although these observed variations are compatible with two layers of anisotropy, they may also indicate deviations of the asthenospheric flow by a relief of lithosphere–asthenosphere boundary beneath the

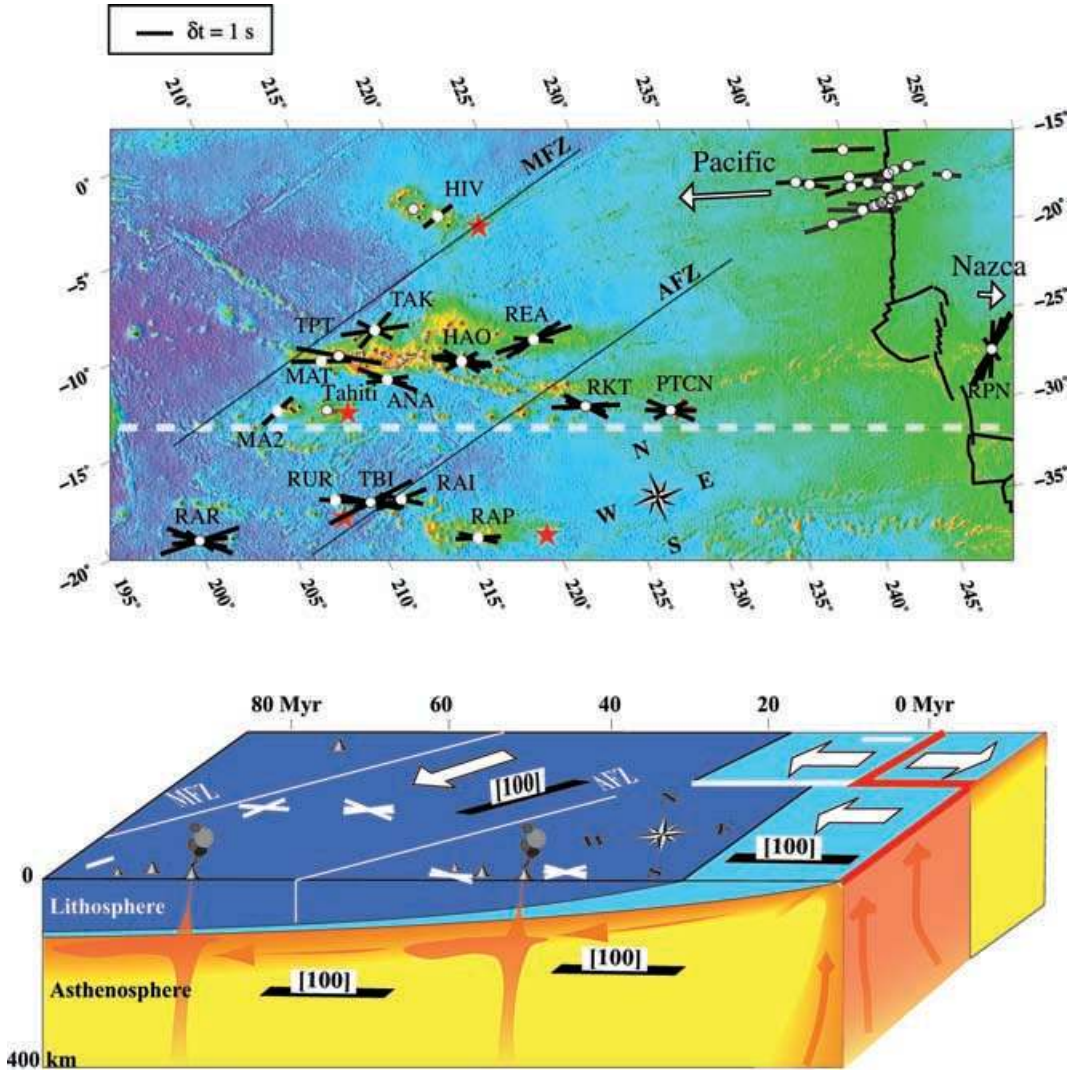

Figure 10. Top: map of individual SKS splitting measurements rotated in the APM reference frame. In this representation, the Pacific Plate moves towards the left. Bottom: Schematic bloc diagram showing an upper mantle cross-section parallel to the present-day Pacific APM direction (roughly parallel to the white doted line on the map). Blue colors represent the lithospheric mantle (light blue = lithosphere younger than 20–25 Myr). This cartoon illustrates one of the best two-layer anisotropic structures that may explain the splitting pattern observed in French Polynesia. Asthenospheric mantle and lithospheric mantle younger than 20–25 Ma are characterized by olivine [100] axes homogeneously oriented parallel to the current Pacific APM direction whereas lithospheric mantle older than 25 Myr has fossilized olivine [100] axes oriented parallel to the palaeoexpansion direction underlined by the Marquesas (MFZ) and Austral (AFZ) fracture zones. White arrows represent the palaeo and present-day expansion direction.

fracture zone. Finally, these steps might also be the site of initiation of instabilities related to small-scale convection (Morency *et al.* 2005).

4.7 Small-scale convection beneath the lithosphere

In the case of a fast moving plate (>10 cm yr^{-1}), Vidal (2004) argued that small-scale convection may induce 2-D steady rolls with radius $\sim$150–300 km aligned along the plate motion direction (Haxby & Weissel 1986; Cazenave *et al.* 1992). The flow path in these rolls is expected to be helicoidal and may induce randomization of olivine fast axis (Montagner 2002). Such small-scale instabilities may, therefore, weaken the anisotropy (Montagner 2002), and lower the delay times in the asthenospheric layer (Harmon *et al.* 2004). At station REA, which is away from the hotspots and the Fracture Zones, the average fast direction is roughly EW. This observation is compatible with the EW channel of low anisotropy observed at 200 km depth by surface wave tomography (Montagner 2002; Maggi *et al.* 2006a) that was interpreted as resulting from small-scale convection beneath the Pacific. This mechanism was also invoked to explain variation of splitting delay times observed on young seafloor (between 5.5—and 7 Ma) near the southern East Pacific Rise (Harmon *et al.* 2004). Small-scale convection may also erode the step in lithospheric thickness associated with the age offset towards the old side of the fracture zone. The influence of the step in lithospheric thickness across a fracture zone should, therefore remain weak. This mechanism was invoked to explain the presence of volcanic islands on the oldest side of the plate near Marquesas Fracture Zone (Sleep 2002).

4.8 Upper mantle apparent isotropy beneath Tahiti

In this study, we went through the whole dataset provided by the two permanent GEOSCOPE and LDG/CEA stations PPT and PPTL

installed on Tahiti and we confirmed the apparent isotropy observed at Tahiti that was already described in several papers during the last decade (Russo & Okal 1998; Wolfe & Silver 1998; Barruol & Hoffmann 1999). We now discuss four possible causes of apparent isotropy beneath Tahiti, taking into account that a combination of several effects is possible.

4.8.1 Vertical olivine [100] axes

The mantle upwelling beneath a hotspot is expected to concentrate the olivine [100] axes close to the vertical direction. This direction being weakly anisotropic within the olivine single crystal (Mainprice *et al.* 2000), this would result in the absence of detectable splitting by the vertically propagating SKS waves (Mainprice & Silver 1993). The upwelling associated to the Society hotspot is rather well resolved in the upper mantle beneath Tahiti by global body wave and surface wave tomography (Montelli *et al.* 2004; Maggi *et al.* 2006b) that show that the minimum radius of this plume-like upwelling is 300 km. Since the center of the present-day location of the active Society hotspot is about 130 km ESE from Tahiti, one can propose that SKS phases recorded at the Tahiti stations sample the Society hotspot mantle upwelling during their propagation in the sublithospheric mantle. However, the analysis of lherzolite xenoliths from Tahiti suggests that the lithosphere should still preserve its anisotropy (Tommasi *et al.* 2004) unless the lithosphere is mechanically eroded.

4.8.2 Two anisotropic layers

The presence of two anisotropic layers, with perpendicular fast axes and similar δt values in each layer, may in principle also result in the absence of detectable anisotropy, the delay acquired within the lower layer being removed by the upper one. Such a structure was proposed for instance at station CAN (Barruol & Hoffmann 1999) and several other stations in Australia (Heintz & Kenneth 2006), but is likely not valid for French Polynesia since the two layers of anisotropy deduced from SKS splitting, surface waves analyses, and from plate tectonics data are clearly not orthogonal to each other.

4.8.3 Presence of melt

The presence of melt in the upper mantle beneath Tahiti may also explain the apparent isotropy. Recent volcanism dated from 1.0 to 0.5 Ma is observed on Tahiti Island and surface wave tomography shows anomalously low upper-mantle velocities beneath the Society hotspot at depths from 50 to 400 km (Maggi *et al.* 2006b). The influence of melt on seismic anisotropy is however debated. On one hand, laboratory experiments suggest that the [100] axis alignment changes in the presence of melt (e.g. Holtzman *et al.* 2003). On the other hand, Vauchez & Garrido (2001) have shown from the analysis of olivine preferred orientation in naturally deformed mantle rocks that the asthenospherization of a lithospheric mantle under static conditions seems to preserve the original olivine preferred orientations and, therefore, should not affect the seismic anisotropy. Finally, petrophysical modelling combining olivine lattice preferred orientation (LPO) and anisometric melt pockets (Vauchez *et al.* 2000) shows the importance of the relative orientation of the melt pockets relative to the solid-state flow microstructure, suggesting that if melt pockets are oriented at high angle to the foliation the two contributions may cancel out, providing an isotropic medium for the direction sampled by the vertically propagating shear wave.

4.8.4 Mantle heterogeneities

The apparent isotropy recorded at Tahiti may finally result from the presence of small-scale heterogeneities beneath the island that might conspire to mask the deformation-induced anisotropic signature. Such heterogeneities in the upper-mantle structure can be related to the magmatism associated to the Society hotspot and/or to small-scale mantle flow variations related to the plume ascent, deflection and spreading.

5 CONCLUSION

Shear wave splitting measurements were conducted on 18 stations in South Pacific and particularly in French Polynesia in the framework of the PLUME experiment. The goal was to better document upper-mantle structure and dynamics beneath this poorly instrumented area. SKS and SKKS phases sampled an oceanic lithosphere with ages varying between 30 and 100 Ma. The observed fast polarization directions, at first order, correlate with the present-day Pacific Plate motion direction, suggesting that the anisotropy is primarily related to the present-day deformation in the asthenosphere beneath the oceanic plate. At few stations, we observe events with fast polarization directions parallel to fracture zones, suggesting that these features may have a long-lasting influence on the observed anisotropy.

We show, however, that the fast shear wave polarization direction Φ depends on event backazimuth and that two layers of anisotropy may explain these variations better than a single layer. Since our backazimuthal coverage is not good enough to obtain a unique two-layer anisotropy model, we combine the observations at the network scale and use additional *a priori* such as the plate motion direction to constrain the fast polarization azimuth in the lower anisotropic layer. Our preferred model favours a lower layer of anisotropy related to asthenospheric flow controlled by the absolute plate motion in the hotspot frame and an upper anisotropic layer in the lithosphere related to the palaeospreading direction between the Pacific and Farallon Plates before 25 Ma (Fig. 10). The presence of a two-layer structure of anisotropy in the South Pacific is consistent with observations of the azimuthal anisotropy of surface waves.

Second-order variations of the measured splitting parameters are not explained by apparent Φ and δt predicted by two-layer models of anisotropy, suggesting other perturbations such as mantle plumes, small-scale convection and complications with asthenospheric flow associated with fracture zones.

Despite the availability of a large amount of data (15 yr) at two permanent stations, no splitting measurements have been obtained on Tahiti Island. This apparent isotropy or weak anisotropy may be related to a complex upper-mantle structure induced by the recent magmatism on Tahiti and/or a vertical-mantle flow beneath this island.

ACKNOWLEDGMENTS

PLUME has been funded by the French Ministère de la Recherche, Action Concertée Incitative (ACI) jeunes chercheurs and by the Ministère de l'Outre Mer. Many thanks to the Centre National de la Recherche Scientifique (CNRS), to the Government of French Polynesia, to the Université de Polynésie Française (UPF), to the Haut-Commissariat de la Polynésie française and to the Commissariat à l'Energie Atomique (CEA) for having made possible this experiment. Thanks to the Global Seismographic Network (particularly IDA and IRIS/IDA from the University of California, San Diego and IRIS/USGS from USGS Albuquerque Seismological

Laboratory) and to GEOSCOPE network (IPG Paris) for the accessibility and the quality of their data. The portable seismic stations were provided by the Institut National des Sciences de l'Univers (INSU), Réseau Large Bande Mobile (RLBM) managed by J. J. Lévèque and J. Burdin (EOPG Strasbourg). We are extremely thankful to Météo France and to the Aviation Civile for having made possible the installation of seismic stations on their sites and for the useful and efficient help provided by their personnel but also by the municipalities of the Polynesian Islands. Many thanks to E. Debayle, Y. Vota, B. Jouanneau, A. Vauchez and C. Zaroli for their help in the experiment. We warmly thank D. Reymond and O. Hyvernaud from the CEA in Tahiti for helpful discussions and their help in providing seismic data. We thank K. Walker and an anonymous reviewer for constructive reviews, M. Sambridge for discussions about model comparison and P. Silver for his splitting analysis code. We used SAC (Lawrence Livermore Nat. Lab) for the seismic analysis and GMT software (SOEST, U. of Hawaïi) for producing the maps.

REFERENCES

Adam, C.R. & Bonneville, A., 2005. Extent of the South Pacific Superswell, *J. Geophys. Res.,* **110,** doi:.

Barruol, G., Silver, P.G. & Vauchez, A., 1997. Seismic anisotropy in the eastern US: deep structure of a complex continental plate, *J. Geophys. Res.,* **102,** 8329–8348.

Barruol, G. & Hoffmann, R., 1999. Seismic anisotropy beneath the Geoscope stations from SKS splitting, *J. Geophys. Res.,* **104,** 10 757–10 774.

Barruol, G. *et al*., 2002. PLUME investigates South Pacific Superswell, *Eos,* **83,** 511–514.

Barruol, G., Reymond, D., Fontaine, F.R., Hyvernaud, O., Maurer, V. & Maamaatuaiahutapu, K., 2006. Characterizing swells in the southern Pacific from seismic and infrasonic noise analyses, *Geophys. J. Int.,* **164,** doi:10.1111/J.1365–246X.2006.02871.x.

Berger, J., Davis, P. & Ekstrom, G., 2004. Ambient Earth noise: a survey of the Global Seismographic Network, *J. Geophys. Res.,* **109,** doi:10.1029/2004JB003408.

Bonneville, A. *et al*., 2002. Arago seamount: the missing hotspot found in the Austral islands, *Geology,* **30,** 1023–1026.

Bromirski, P.D. & Duennebier, F.K., 2002. The near-coastal microseism spectrum: spatial and temporal wave climate relationships, *J. Geophys. Res.,* **107,** doi:10.1029/2001JB000265.

Brousse, R., Barsczus, H.G., Bellon, H., Cantagrel, J.-M., Diraison, C., Guillou, H. & Léotot, C., 1990. Les Marquises (Polynésie française): volcanologie, géochronologie, discussion d'un modèle de point chaud, *Bull. Soc. geol. France,* **6,** 933–949.

Cazenave, A., Houry, S., Lago, B. & Dominh, K., 1992. Geosat-derived geoid anomalies at medium wavelength, *J. Geophys. Res.,* **97,** 7081–7096.

Chevrot, S., 2000. Multichannel analysis of shear wave splitting, *J. Geophys. Res.,* **105,** 21 579–21 590.

Clouard, V., Bonneville, A. & Gillot, P.Y., 2003. The Tarava seamounts: a newly characterized hotspot chain on the south Pacific superswell, *Earth Planet. Sci. Lett.,* **207,** 117–130.

Clouard, V. & Bonneville, A., 2005. Ages of seamounts, islands and plateaus on the Pacific plate, *Geol. Soc. Am. Bull.,* **388,** 71–90.

Diraison, C., Bellon, H., Léotot, C., Brousse, R. & Barsczus, H.G., 1991. L'alignement de la Société (Polynésie Française): volcanologie, géochronologie, proposition d'un modèle de point chaud, *Bull. Soc. geol. France,* **162,** 479–496.

Dumoulin, C., Doin, M.P. & Fleitout, L., 2001. Numerical simulations of the cooling of an oceanic lithosphere above a convective mantle, *Phys. Earth Planet. Int.,* **125,** 45–64.

Duncan, R.A. & McDougall, I., 1974. Migration of volcanism in time in the Marquesas islands, French Polynesia, *Earth Planet. Sci. Lett.,* **21,** 414–420.

Duncan, R.A. & McDougall, I., 1976. Linear volcanism in French Polynesia, *J. Volc. Geotherm. Res.,* **1,** 197–227.

Duncan, R.A. & Richards, M.A., 1991. Hotspots, mantle plumes, flood basalts, and true polar wander, *Rev. Geophys.,* **29,** 31–50.

Dupuy, C., Vidal, P., Maury, R.C. & Guille, G., 1993. Basalts from Mururoa, Fangataufa and Gambier islands (French Polynesia): Geochemical dependence on the age of the lithosphere, *Earth Planet. Sci. Lett.,* **117,** 89–100.

Ekström, G. & Dziewonski, A.M., 1998. The unique anisotropy of the Pacific upper mantle, *Nature,* **394,** 168–172.

Fontaine, F.R., Hooft, E.E.E., Burkett, P.G., Toomey, D.R., Solomon, S.C. & Silver, P.G., 2005. Shear-wave splitting beneath Galápagos archipelago, *Geophys. Res. Lett.,* **32,** doi:10.1029/2005GL024014.

Fowler, C.M.R., 1990. *The Solid Earth. An Introduction to Global Geophysics*, Cambridge University Press, Cambridge, 472 pp.

Francis, T.J.G., 1969. Generation of seismic anisotropy in the upper mantle along the mid-oceanic ridges, *Nature,* **221,** 162–165.

Grand, S., Van Der Hilst, R. & Widiyantoro, S., 1997. Global seismic tomography: a snapshot of convection in the Earth, *GSA Today,* **7,** 1–7.

Gripp, A.E. & Gordon, R.B., 2002. Young tracks of hotspots and current plate velocities, *Geophys. J. Int.,* **150,** 321–361.

Hall, S.A., Kendall, J.M. & Van Der Baan, M., 2004. Some comments on the effects of lower-mantle anisotropy on SKS and SKKS phases, *Phys. Earth Planet. Int.,* **146,** doi:10.1016/j.pepi.2005.05.002.

Hammond, J.O.S., Kendall, J.M., Rümpker, G., Wookey, J., Teanby, N., Joseph, P., Ryberg, T. & Stuart, G., 2005. Upper mantle anisotropy beneath the Seychelles microcontinent, *J. Geophys. Res.,* **110,** doi:10.1029/2005JB003757.

Harmon, N., Forsyth, D.A. & Fischer, K.M., 2004. Variations in shear wave splitting in young Pacific seafloor, *Geophys. Res. Lett.,* **31,** doi:10.1029/2004GL020495.

Hartog, R. & Schwartz, S., 2001. Depth-dependent mantle anisotropy below the San Andreas fault system: apparent splitting parameters and waveforms, *J. Geophys. Res.,* **106,** 4155–4167.

Hasselmann, K., 1963. A statistical analysis of the generation of microseisms, *Rev. Geophys.,* **1,** 177–210.

Haxby, W. & Weissel, J., 1986. Evidence for small-scale mantle convection from SEASAT altimeter data, *J. Geophys. Res.,* **91,** 3507–3520.

Heintz, M. & Kenneth, B.L.N., 2006. The apparent isotropic Australian upper mantle, *Geophys. Res. Lett.,* **33,** doi:10.1029/2006GL026401.

Hess, H.H., 1964. Seismic anisotropy of the uppermost mantle under oceans, *Nature,* **203,** 629–631.

Holtzman, B.K., Kholstedt, D.L., Zimmerman, M.E., Heidelbach, F., Hiraga, T. & Hustoft, J., 2003. Melt segregation and strain partitioning: implication for seismic anisotropy and mantle flow, *Science,* **301,** 1227–1230.

Ito, G., McNutt, M.K. & Gibson, R.L., 1995. Crustal structure of the Tuamotu plateau, 15°S, and implication for its origin, *J. Geophys. Res.,* **100,** 8097–8114.

Jordahl, K.A., Caress, D.W., McNutt, M.K. & Bonneville, A., 2004. Seafloor morphology of the South Pacific Superswell region, in *Oceanic Hot Spots*, pp. 9–28, eds Hekinian, R., Stoffers, P. & Cheminée, J.L., Springer Verlag, Berlin, Heidelberg.

Kaminski, E. & Ribe, N.M., 2002. Timescale for the evolution of seismic anisotropy in mantle flow, *Geochem. Geophys. Geosyst.,* **3,** doi:10.1029/2001GC000222.

Kennett, B.L.N. & Engdahl, E.R., 1991. Traveltimes for global earthquake location and phase identification, *Geophys. J. Int.,* **105,** 429–465.

Longuet-Higgins, M.S., 1950. A theory of the origin of the microseisms, *Phil. Trans. Roy. Soc.,* **243,** 1–35.

Maggi, A., Debayle, E., Priestley, K. & Barruol, G., 2006a. Azimuthal anisotropy of the Pacific region, *Earth Planet. Sci. Lett.,* **250,** 53–71, doi:10.1016/j.epsl.2006.07.010.

Maggi, A., Debayle, E., Priestley, K. & Barruol, G., 2006b. Multi-mode surface waveform tomography of the Pacific ocean: a closer look at the lithopsheric cooling signature, *Geophys. J. Int.,* **166,** doi:10.1111/j.1365–246X.2006.03037.x.

Mainprice, D. & Silver, P.G., 1993. Interpretation of *SKS*-waves using samples from the subcontinental lithosphere, *Phys. Earth Planet. Int.,* **78,** 257–280.

Mainprice, D., Barruol, G. & Ben Ismail, W., 2000. The seismic anisotropy of the Earth's mantle: from single crystal to polycrystal, in *Earth's Deep Interior: Mineral Physics and Tomography from the Atomic to the Global Scale*, pp. 237–264, ed. Karato, S.I., AGU, Washington, DC.

Mammerickx, J. & Sharman, G.F., 1988. Tectonic evolution of the North Pacific during the Cretaceous quiet period, *J. Geophys. Res.,* **93,** 3009–3024.

Mayes, C.L., Lawver, L.A. & Sandwell, D.T., 1990. Tectonic history and new isochron chart of the South Pacific, *J. Geophys. Res.,* **95,** 8543–8567.

McNamara, D.E. & Buland, R., 2004. Ambient noise levels in the continental United States, *Bull. Seismol. Soc. Am.,* **94,** 1517–1527.

McNutt, M.K., Sichoix, L. & Bonneville, A., 1996. Modal depths from shipboard bathymetry: there is a south Pacific Superswell, *Geophys. Res. Lett.,* **23,** 3397–3400.

McNutt, M.K., 1998. Superswells, *Rev. Geophys.,* **36,** 211–244.

Mégnin, C. & Romanowicz, B.A., 2000. A 3D model of shear velocity in the mantle from the inversion of waveforms of body, surface, and higher mode waveforms, *Geophys. J. Int.,* **143,** 708–728.

Montagner, J.P., 1985. Seismic anisotropy of the Pacific ocean inferred from long-period surface waves dispersion, *Phys. Earth Planet. Int.,* **38,** 28–50.

Montagner, J.P. & Tanimoto, T., 1991. Global upper mantle tomography of seismic velocities and anisotropies, *J. Geophys. Res.,* **96,** 20 337–20 351.

Montagner, J.P., 2002. Upper mantle low anisotropy channels below the Pacific plate, *Earth Planet. Sci. Lett.,* **202,** 263–274.

Montelli, R., Nolet, G., Dahlen, F.A., Masters, G., Engdahl, E.R. & Hung, S.H., 2004. Finite-frequency tomography reveals a variety of plumes in the mantle, *Science,* **303,** 338–343.

Morency, C., Doin, M.P. & Dumoulin, C., 2005. Three-dimensional numerical simulations of mantle flow beneath mid-ocean ridges, *J. Geophys. Res.,* **110,** doi:10.1029/2004JB003454.

Müller, R.D., Roest, W.R., Royer, J.Y., Gahagan, L.M. & Sclater, J.G., 1997. Digital isochrons of the world's ocean floor, *J. Geophys. Res.,* **102,** 3211–3214.

Nicolas, A. & Christensen, N.I., 1987. Formation of anisotropy in upper mantle peridotites-A review, in *Composition, Structure and Dynamics of the Lithosphere-Asthenosphere System*, pp. 111–123, eds Fuchs, K. & Froidevaux, C., AGU, Washington, DC.

Nishimura, C.E. & Forsyth, D.W., 1988. Rayleigh wave phase velocities in the Pacific with implications for azimuthal anisotropy and lateral heterogeneities, *Geophys. J.,* **94,** 479–501.

Nishimura, C.E. & Forsyth, D.W., 1989. The anisotropic structure of the upper mantle in the Pacific, *Geophys. J.,* **96,** 203–209.

Niu, F. & Perez, A., 2004. Seismic anisotropy in the lower mantle: a comparison of waveform splitting of SKS and SKKS, *Geophys. Res. Lett.,* **31,** doi:10.1029/2004GL021196.

Peterson, J., 1993. Observation and modeling of seismic background noise, *U.S. Geol. Surv. Open File Rep.,* **93–322,** 1–95.

Raitt, R.W., Shor, G.G., Francis, T.J.G. & Morris, G.B., 1969. Anisotropy of the Pacific upper mantle, *J. Geophys. Res.,* **74,** 3095–3109.

Ribe, N.M. & Christensen, U.R., 1994. Three-dimensional modeling of plume-lithosphere interaction, *J. Geophys. Res.,* **99,** 669–682.

Ribe, N.M. & Christensen, U., 1999. The dynamical origin of Hawaiian volcanism, *Earth Planet. Sci. Lett.,* **171,** 517–531.

Rümpker, G., Tommasi, A. & Kendall, J.M., 1999. Numerical simulations of depth-dependent anisotropy and frequency-dependent wave propagation effects, *J. Geophys. Res.,* **104,** 23 141–23 154.

Russo, R. & Okal, E., 1998. Shear wave splitting and upper mantle deformation in French Polynesia: Evidence for small-scale heterogeneity related to the Society hotspot, *J. Geophys. Res.,* **103,** 15 089–15 107.

Schubert, G., Froidevaux, C. & Yuen, D.A., 1976. Oceanic lithosphere and asthenosphere: thermal and mechanical structure, *J. Geophys. Res.,* **81,** 3525–3540.

Schulte-Pelkum, V., Masters, G. & Shearer, P.M., 2001. Upper mantle anisotropy from long-period P polarization, *J. Geophys. Res.,* **106,** 21 917–21 934.

Shimamura, H. & Asada, T., 1983. Velocity anisotropy extending over the entire depth of the oceanic lithosphere, in *Geodynamics of the Western Pacific – Indonesian Region*, pp. 105–120, eds Hilde, T.W.C. & Uyeda, S., American Geophysical Union, Washington, DC.

Sichoix, L., Bonneville, A. & McNutt, M.K., 1998. The seafloor swells and Superswell in French Polynesia, *J. Geophys. Res.,* **103,** 27 123–27 133.

Silver, P.G. & Chan, W.W., 1988. Implications for continental structure and evolution from seismic anisotropy, *Nature,* **335,** 34–39.

Silver, P.G. & Chan, W.W., 1991. Shear wave splitting and subcontinental mantle deformation, *J. Geophys. Res.,* **96,** 16 429–16 454.

Silver, P.G. & Savage, M.K., 1994. The interpretation of shear-wave splitting parameters in the presence of two anisotropic layers, *Geophys. J. Int.,* **119,** 949–963.

Silver, P.G., Gao, S.S. & Kaapvaal seismic group, 2001. Mantle deformation beneath southern Africa, *Geophys. Res. Lett.,* **28,** 2493–2496.

Sleep, N.H., 1990. Hotspots and mantle plumes: some phenomology, *J. Geophys. Res.,* **95,** 6715–6736.

Sleep, N.H., 1994. Lithospheric thinning by midplate mantle plumes and the thermal history of hot plume material ponded at sublithospheric depth, *J. Geophys. Res.,* **99,** 9327–9343.

Sleep, N.H., 2002. Local lithospheric relief associated with fracture zones and ponded plume material, *Geochem. Geophys. Geosyst.,* **3,** doi:10.1029/2002GC000376.

Smith, D.B., Ritzwoller, M.H. & Shapiro, N.M., 2004. Stratification of anisotropy in the Pacific upper mantle, *J. Geophys. Res.,* **109,** doi:10.1029/2004JB003200.

Smith, W.H.F. & Sandwell, D.T., 1994. Bathymetric prediction from dense satellite altimetry and sparse shipboard bathymetry, *J. Geophys. Res.,* **99,** 21 803–21 824.

Stutzmann, E., Roult, G. & Astiz, L., 2000. GEOSCOPE station noise levels, *Bull. Seismol. Soc. Amer.,* **90,** 690–701.

Su, L. & Park, J., 1994. Anisotropy and the splitting of *PS* waves, *Phys. Earth Planet. Int.,* **86,** 263–276.

Su, W.J., Woodward, R.L. & Dziewonski, A.M., 1994. Degree 12 model of shear velocity heterogeneity in the mantle, *J. Geophys. Res.,* **99,** 6945–6980.

Suetsugu, D. *et al*., 2005. Probing South Pacific mantle plumes with Broadband OBS, *Eos,* **86,** 429–435.

Talandier, J. & Kuster, G.T., 1976. Seismicity and submarine volcanic activity in French Polynesia, *J. Geophys. Res.,* **81,** 936–948.

Thoraval, C., Tommasi, A. & Doin, M.P., 2006. Plume-lithosphere interaction beneath a fast moving plate, *Geophys. Res. Lett.,* **33,** doi:10.1029/2005GL024047.

Tommasi, A., 1998. Forward modeling of the development of seismic anisotropy in the upper mantle, *Earth Planet. Sci. Lett.,* **160,** 1–13.

Tommasi, A., Godard, M., Coromina, G., Dautria, J.M. & Barsczus, H., 2004. Seismic anisotropy and compositionally induced velocity anomalies in the lithosphere above mantle plumes: a petrological and microstructural study of mantle xenoliths from French Polynesia, *Earth Planet. Sci. Lett.,* **227,** 539–556.

Trampert, J. & Woodhouse, J.H., 2003. Global anisotropic phase velocity maps for fundamental mode surface waves between 40 and 150s, *Geophys. J. Int.,* **154,** 154–165.

Van Der Hilst, R.D., Widiyantoro, S. & Engdahl, E.R., 1997. Evidence for deep mantle circulation from global tomography, *Nature,* **386,** 578–584.

Vauchez, A., Tommasi, A., Barruol, G. & Maumus, J., 2000. Upper mantle deformation and seismic anisotropy in continental rifts, *Phys. Chem. Earth,* **25,** 111–117.

Vauchez, A. & Garrido, C., 2001. Seismic properties of an asthenospherized lithospheric mantle: constraints from lattice preferred orientations in peridotite from the Ronda Massif, *Earth Planet. Sci. Lett.,* **192,** 245–259.

Vidal, V., 2004. Interaction des Différentes échelles de Convection dans le Manteau Terrestre, *PhD thesis*, University of Paris VI, 270 pp.

Vinnik, L.P., Kosarev, G.L. & Makeyeva, L.I., 1984. Anisotropiya litosfery po nablyudeniyam voln SKS and SKKS, *Dokl. Akad. Nauk. USSR,* **278,** 1335–1339.

Vinnik, L.P., Makeyeva, L.I., Milev, A. & Usenko, A.Y., 1992. Global patterns of azimuthal anisotropy and deformations in the continental mantle, *Geophys. J. Int.,* **111,** 433–437.

Viso, R.F., Larson, R.L. & Pockalny, R.A., 2005. Tectonic evolution of the Pacific-Phoenix-Farallon triple junction in the South Pacific ocean, *Earth Planet. Sci. Lett.,* **233,** doi:10.1016/j.epsl.2005.02.004.

Waite, G.P. & Schutt, D.L., 2005. Models of lithosphere and asthenosphere anisotropic structure of the Yellowstone hot spot from shear wave splitting, *J. Geophys. Res.,* **110,** doi:10.1029/2004JB003501.

Walker, K.T., Bokelmann, G.H.R. & Klemperer, S.L., 2001. Shear-wave splitting to test mantle deformation models around Hawaii, *Geophys. Res. Lett.*, **28**, 4319–4322.

Walker, K.T., Nyblade, A.A., Klemperer, S.L., Bokelmann, G.H.R. & Owens, T.J., 2004. On the relationship between extension and anisotropy: constraints from shear wave splitting across the East African Plateau, *J. Geophys. Res.,* **109,** doi:10.1029/2003JB002866.

Walker, K.T., Bokelmann, G.H.R., Klemperer, S.L. & Bock, G., 2005a. Shear-wave splitting around the Eifel hotspot: evidence for a mantle upwelling, *Geophys. J. Int.,* **163,** doi: 10.1111/j.1365–246X.2005.02636.x.

Walker, K.T., Bokelmann, G.H.R., Klemperer, S.L. & Nyblade, A.A., 2005b. Shear-wave splitting around hotspots: evidence for upwelling-related mantle flow?, in *Plates, Plumes and Paradigms*, eds Foulger, G.R., Natland, J.H., Presnall, D.C. & Anderson, D.L., Geological Society of America, doi:10.1130/2005.2388(11).

Wolfe, C. & Silver, P.G., 1998. Seismic anisotropy of oceanic upper mantle: Shear wave splitting methodologies and observations, *J. Geophys. Res.,* **103,** 749–771.

Wolfe, C.J. & Solomon, S.C., 1998. Shear wave splitting and implication for mantle flow beneath the MELT region of the East Pacific Rise, *Science,* **280,** 1230–1232.

APPENDIX A

The seismic stations installed for the PLUME experiment consist of broad-band Streckeisen STS-2 sensors, which are characterized by a flat velocity response from 40 Hz to 120 s, connected to TITAN-Agecodagis recording systems. They recorded continuously on two independent channels at rates of 40 and 1.25 samples per second. The first channel is primarily dedicated to body wave analysis and the second one to surface wave analysis. Most sensors were set up on a 20 cm thick layer of concrete, in a 1 m deep hole, and oriented in the geographic reference frame, taking into account the local magnetic declination that can be up to 15° in French Polynesia. In order to insulate the sensor from diurnal thermal variations, it was covered by an insulating jacket and by a 10 cm thick Styrofoam box. The box was itself covered by a layer of 30–50 cm of sand. There are, however, some exceptions to this instrumental setup: station HAO in the Tuamotu archipelago was installed inside an abandoned building of the airport and station RAP on Rapa Island (in Austral archipelago) was installed in a small hut on the *Météo France* site. In both cases, the sensor was sited directly on a concrete floor and covered by the insulating jacket and the Styrofoam box.

The long period Laboratoire de Géophysique/ Commissariat à l'Energie Atomique (LDG/CEA) permanent stations (Fig. 1 and Table 1) are installed in Tahiti (PPTL), Tubuai (TBI, Austral islands) and Rikitea (RKT, Gambier Islands). They are equipped with 60 s long-period velocity sensors designed by LDG/CEA that sample the data at 4 Hz. The Tahiti station PPTL is part of the CTBT (Comprehensive Nuclear Test Ban Treaty) organization network. This station was certified several years ago, on criteria including noise level, seismic vault construction, energy, 24-bit digitizer, and good horizontal seismometer orientation. This high-quality station has been running for more than 15 yr.